RESEARCH ARTICLE | FEBRUARY 23 2024

# A user-centered smart inhaler algorithm for targeted drug delivery in juvenile onset recurrent respiratory papillomatosis treatment integrating computational fluid particle dynamics and machine learning ⓢⒻ✅

Mohammad Rashedul Islam ⓘ ; Chenang Liu ⓘ ; Changjie Cai ⓘ ; Jindal Shah ⓘ ; Yu Feng ✉ ⓘ

🔴 Check for updates

View Online     Export Citation     CrossMark

# A user-centered smart inhaler algorithm for targeted drug delivery in juvenile onset recurrent respiratory papillomatosis treatment integrating computational fluid particle dynamics and machine learning F SCI

Mohammad Rashedul Islam,[1] iD Chenang Liu,[2] iD Changjie Cai,[3] iD Jindal Shah,[1] iD and Yu Feng[1,a] iD

**AFFILIATIONS**

[1]School of Chemical Engineering, Oklahoma State University, Stillwater, Oklahoma 74078, USA
[2]School of Industrial Engineering and Management, Oklahoma State University, Stillwater, Oklahoma 74078, USA
[3]The University of Oklahoma Health Sciences Center, Oklahoma City, Oklahoma 73126, USA

[a]**Present address:** 420 Engineering North, Stillwater, Oklahoma 74078, USA. **Author to whom correspondence should be addressed:** yu.feng@okstate.edu. **Tel.:** (405)744-7441

**ABSTRACT**

Recurrent respiratory papillomatosis (RRP) is a chronic condition primarily affecting children, known as juvenile onset RRP (JORRP), caused by a viral infection. Antiviral medications have been used to reduce the need for frequent surgeries, slow the growth of papillomata, and prevent disease spread. Effective treatment of JORRP necessitates targeted drug delivery (TDD) to ensure that inhaled aerosolized drugs reach specific sites, such as the larynx and glottis, without harming healthy tissues. Using computational fluid particle dynamics (CFPD) and machine learning (ML), this study (1) investigated how drug properties and individual factors influence TDD efficiency for JORRP treatment and (2) developed personalized inhalation therapy using an ML-empowered smart inhaler control algorithm for precise medication release. This algorithm optimizes the inhaler nozzle position and diameter based on drug and patient-specific data, enhancing drug delivery to the larynx and glottis. CFPD simulations show that particle size significantly affects deposition fractions in the upper airway, emphasizing the importance of particle size selection. Additionally, optimal nozzle diameter and delivery efficiency depend on particle size, inhalation flow rate, and release time. The ML-based TDD strategy, employing a classification and regression tree model, outperforms conventional inhalation therapy by achieving a higher delivery efficiency to the larynx and glottis. This innovative concept of an ML-empowered smart inhaler represents a promising step toward personalized and precise pulmonary healthcare through inhalation therapy. It demonstrates the potential of AI-driven smart inhalers for improving the treatment outcomes of lung diseases that require TDD at designated lung sites.

*Published under an exclusive license by AIP Publishing.* https://doi.org/10.1063/5.0186786

## NOMENCLATURE
### Acronyms

| | |
|---|---|
| CART | Classification and regression trees |
| CFPD | Computational fluid particle dynamics |
| CFC | Chlorofluorocarbon |
| CHAID | Chi-squared automatic interaction detector |
| $CO_2$ | Carbon dioxide |
| CPRT | Controlled particle release and targeting |
| CV | Cross-validation |
| DF | Deposition fraction |
| DL | Deep learning |
| DPI | Dry powder inhaler |
| DPM | Discrete phase model |
| DT | Decision tree |
| GPR | Gaussian process regression |
| HPV | Human papillomavirus |
| ID3 | Iterative dichotomiser 3 |
| JORRP | Juvenile onset recurrent respiratory papillomatosis |
| KTP | Potassium titanyl phosphate |

| | |
|---|---|
| MAE | Mean absolute error |
| ML | Machine learning |
| MSE | Mean squared error |
| N-S | Navier–Stokes equations |
| pMDI | Pressurized metered dose inhaler |
| RRR | Recurrent respiratory papillomatosis |
| RD | Relative difference |
| RF | Random forest |
| $R^2$ | Coefficient of determination |
| SST | Shear stress transport |
| SVM | Support vector machine |
| TB | Tracheobronchial |
| TDD | Targeted drug delivery |
| TDS | Targeted delivery strategy |

## Symbols

| | |
|---|---|
| $C_D$ | Drag coefficient |
| $C_c$ | Cunningham correction factor |
| $d_p$ | Particle diameter |
| $D_{in}$ | Hydraulic diameter of the mouth opening |
| $D_{nozzle}$ | Optimal particle release nozzle diameter for targeted delivery |
| $d_{ij}$ | Deformation rate |
| $\vec{F}_D$ | Drag force |
| $\vec{F}_g$ | Gravity |
| $F_{L,i}$ | Saffman lift force |
| $\vec{g}_i$ | Gravitational acceleration |
| $i(t)$ | Impurity function |
| $K$ | Constant coefficient of Saffman lift force |
| $M$ | Number of variables |
| $m_p$ | Particle mass |
| $N$ | Observations |
| $p$ | Pressure |
| $P_l$ | Probabilities of the left nodes |
| $P_r$ | Probabilities of the right nodes |
| $Q$ | Transient inhalation–exhalation flow rate |
| $Q_{in}$ | Average inhalation flow rate |
| $Q_{max}$ | Peak inhalation flow rate |
| $Re_{in}$ | Inlet Reynolds number |
| $Re_p$ | Particle Reynolds number |
| $S$ | Ratio of particle density to fluid density |
| $T$ | Total inhalation–exhalation time |
| $t_c$ | Left and right child nodes |
| $t_p$ | Parent node |
| $\vec{u}_f$ | Airflow velocity |
| $\left\|\vec{u}_f\right\|_{Critical}$ | Critical air velocity magnitude for iso-surface generation |
| $\vec{u}_p$ | Particle velocity |
| $(x_c, y_c, z_c)$ | Optimal nozzle center coordinate for targeted delivery |
| $x_R^j$ | Best splitting value |
| $\bar{y}$ | Mean of actual value |
| $y_i$ | Actual value of dependent variable |
| $\hat{y}_i$ | Predicted value of dependent variable |

## Greek symbols

| | |
|---|---|
| $\lambda$ | Mean free path of air |
| $\Delta i(t)$ | Change of impurity function |
| $\mu$ | Air dynamic viscosity |
| $\nu$ | Kinematic viscosity |
| $\rho$ | Air density |
| $\rho_p$ | Particle density |
| $\tau_{ij}$ | Viscous stress tensor |

## I. INTRODUCTION

Recurrent respiratory papillomatosis (RRP) is a clinical syndrome with a viral origin that affects both adults and children, causing the development of papilloma in the respiratory system.[1] It is a disease mainly caused by human papillomavirus (HPV) types 6 or 11, resulting in exophytic lesions throughout the human respiratory airways, most commonly the larynx and glottis.[2] Although tumors resulting from RRP are mostly benign, the malignant possibility and fatality rate become much higher in children, accompanied by rapid exacerbation of the disease. The disease is also called juvenile onset RRP (JORRP), which is more aggressive than adult-onset RRP.[3,4]

Finding an effective clinical therapy for JORRP is still challenging due to a high propensity for recurrence and unsolvable complications.[5,6] Surgery using photoangiolytic lasers, including the 532 nm potassium titanyl phosphate (KTP) laser and the carbon dioxide ($CO_2$) laser, are the most frequently used techniques.[7,8] However, the recurrent nature of JORRP carries the risk of iatrogenic and general anesthesia consequences and thermal tissue damage from laser treatment.[9] In this context, adjuvant antiviral medications have been prescribed over the past decade and researched for potential therapeutic uses.[10] Several adjuvant medicines can be used to avoid blockage throughout the infection.[11] The primary criteria for adjuvant therapy include more than four surgeries per year due to the growth of papillomata that compromise the airways or the spread of disease to multiple locations in the airway.[12–15] Other antiviral drugs, such as acyclovir, cidofovir, and ribavirin, hold potential as additional adjuvant therapies to reduce treatment resistance.[2] The goal of utilizing different vaccines is to both prevent and treat RRP. There is limited proof to show the effectiveness of these adjuvant methods, vaccines, and chemotherapy, and none entirely stop the growth of the tumors.

Inhalation therapy can also be used to deliver specific medications to the larynx and glottis areas to help control tumor growth and JORRP exacerbation. This may include the use of medications such as interferon, cidofovir, or 5-fluorouracil. However, conventional inhalation therapy will generate undesired deposition on healthy tissues through the pulmonary route, reducing the therapeutic effectiveness and leading to side effects. Such side effects can be complicated for children and adolescents to tolerate. Ineffective drug delivery can also result in the recurrence of JORRP tumors, which will need for ongoing treatment and the possibility of further complications. Therefore, targeted drug delivery (TDD) to the designated sites in the upper airway is necessary for JORRP treatment.

Computational fluid particle dynamics (CFPD) can be used to predict air-particle flow dynamics in lung airways. This approach has been employed for decades to enhance the fundamental understanding of the complex mechanisms involved in respiratory drug delivery.[16] Based on first principles, experimentally validated CFPD models can significantly reduce the time and expense required to develop new targeted delivery strategies, by providing high-resolution spatiotemporal distributions of pulmonary air-particle flow variables of interest. CFPD

research efforts have been made to achieve pulmonary targeted drug delivery, such as the controlled particle release and targeting (CPRT) strategy, introduced by Kleinstreuer and Zhang.[17] Specifically, by using the particle "backtracking" method,[17] CPRT can link the particle deposition locations with their release positions at the mouth front to find the precise particle release coordinates to deliver the drug particles to designated lung sites. The research[17] confirms a significant increase in particle delivery efficiency for the targeted region in lung airways using CPRT than conventional inhalation therapy. Another CFPD study used a similar CPRT concept to achieve lobe-specific drug delivery. It showed that using the targeted delivery strategy, lobe-specific drug delivery can be enhanced up to 90% when the releasing position and velocity of the drug particles were fine-tuned using CPRT compared with the conventional inhalation therapy.[18] Additionally, drug delivery via the pulmonary route has been combined with charged substances to achieve targeted delivery and improve aerosol deposition utilizing external magnetic fields that were delivered externally.[19–22] Another CFPD study introduced a novel inhalation therapy of a short-pulsed bolus of aerosolized drug particles.[23] The study claimed that this drug delivery method can lead to drug delivery efficiency to small airways (i.e., G7 and above) higher than 68%. Recently, Islam and Feng[24] employed the CPRT concept and explored an innovative approach to treat small airway tumors by administering aerosolized chemotherapeutic particles via endotracheal catheters, focusing on achieving the targeted delivery to tumor sites. Using CFPD, it shows significantly improved drug delivery efficiencies to tumors located at G10, offering a promising alternative to conventional therapies. Wang et al.[25] focused on improving the drug delivery efficiency for COVID-19 treatment through targeted inhalation therapy. Utilizing a patient-specific tracheobronchial tree model and computational fluid dynamics, they optimized point-source aerosol release locations, resulting in 3.2 times increase in deposition efficiency to specific lung regions affected by COVID-19, with minimal impact on overall drug delivery efficiency.

A couple of factors can make the targeted delivery to specific regions in the pulmonary route challenging. It is commonly observed that children and adult patients with serious lung conditions may face difficulty in producing enough inspiratory airflow to carry sufficiently high dose into designated lung sites, since a strong inhalation is required to fluidize the drug powders and produce an appropriate amount of therapeutic aerosols.[26] In addition, it is quite challenging for physicians to comprehend how a patient with pulmonary diseases operates inhalers in practice when they are not in clinic.[27] The inhaler misuse can be either unintentional or planned. In reality, healthcare professional often overestimate patient adherence to their medications using correct patient–inhaler coordination.[28] Therefore, inadequate inhalation practice and low adherence to the prescribed personalized treatment are two major factors in respiratory disease control failure among patients. This has consistently been linked to poor drug delivery efficiency, decreased living standard, and increased healthcare expenses.[29] In other words, the intersubject variabilities and inconsistencies in breathing patterns (e.g., preferred inhalation flow rate) can significantly influence the drug delivery efficiency.

To address the issues of intersubject variabilities affecting delivery efficiency, the concept of "smart inhalers" has been introduced. These inhalers incorporate sensors to gather data on inhaler usage patterns and patient metrics, offering personalized feedback based on usage timing, inhalation technique, peak flow metrics, or survey outcomes. Numerous studies have indicated that when patients use smart inhalers, there is a notable increase in adherence, a significant decrease in exacerbation rates, and enhanced lung function.[30,31] While some improvement in therapeutic effect is observed with smart inhaler use, the efficacy of drug delivery primarily hinges on the number of therapeutic particles delivered to the targeted sites. Thus, beyond merely collecting patient data, smart inhalers should leverage these data to fine-tune the release and transport of aerosolized particles, aiming for precise drug delivery to specific regions, like the larynx and glottis for JORRP treatment, while minimizing drug deposition on healthy tissues.

Therefore, the goal of this study is to develop a machine learning (ML) algorithm enabled by CFPD that can be integrated into a novel smart inhaler to effectively target the diseased region (i.e., larynx and glottis) for JORRP treatment as an example with minimum particle deposition on healthy tissues. This is achieved by automatically adjusting the drug release nozzle based on patient-specific breathing characteristics (i.e., inhalation flow rate) and inhaled drug properties (i.e., particle diameter). Based on the collected patient-specific information, the ML algorithm aims to automatically find the optimized nozzle location as well as the nozzle diameter that can maximize drug particle delivery to the larynx and glottis region, enhancing the JORRP treatment and reducing side effects. The ML algorithm is trained and tested using data generated by experimentally validated CFPD simulations of drug transport and deposition in a subject-specific human upper airway geometry representing a 6-year-old child. Figure 1 shows how CFPD is used to prepare the dataset depending on the different parameters and how ML algorithm is being trained and tested based on the CFPD dataset. During the implementation of the ML algorithm, the signal acquisition system in the smart inhaler collects patient breathing profiles and particle sizes as inputs first. Then, the ML algorithm outputs the optimized nozzle diameter and location as well as particle release time. These data will be sent to the automatic nozzle adjustment system, which relocate the nozzle and releases the drug particles when the patient inhales again. Figure 2 provides more details explaining how the user-centered smart inhaler integrates with patient-specific and medication-specific data and the ML algorithm. The long-term goal is an AI-empowered user-centered smart inhaler that can effectively target the diseased region with a high degree of precision, providing a safer and more effective treatment option on a patient-specific and medication-specific level. As far as we are aware, the concept of an ML-empowered smart inhaler has not yet been applied in targeted drug delivery for lung disease treatment. Hence, this study represents a first-of-its-kind effort in developing an ML algorithm to support targeted delivery using inhalation therapy for lung diseases, aiming to revolutionize precision medicine by enhancing treatment efficacy and reducing side effects in pulmonary healthcare.

## II. METHODOLOGY
### A. Geometry and mesh

As shown in Figs. 3(a) and 3(b), a subject-specific mouth-to-trachea geometry[32] is employed in this study, which was scaled to a representative size of upper airways for 6-year-old children. A circular mouth opening with a hydraulic diameter $D_{in} = 10$ mm is considered
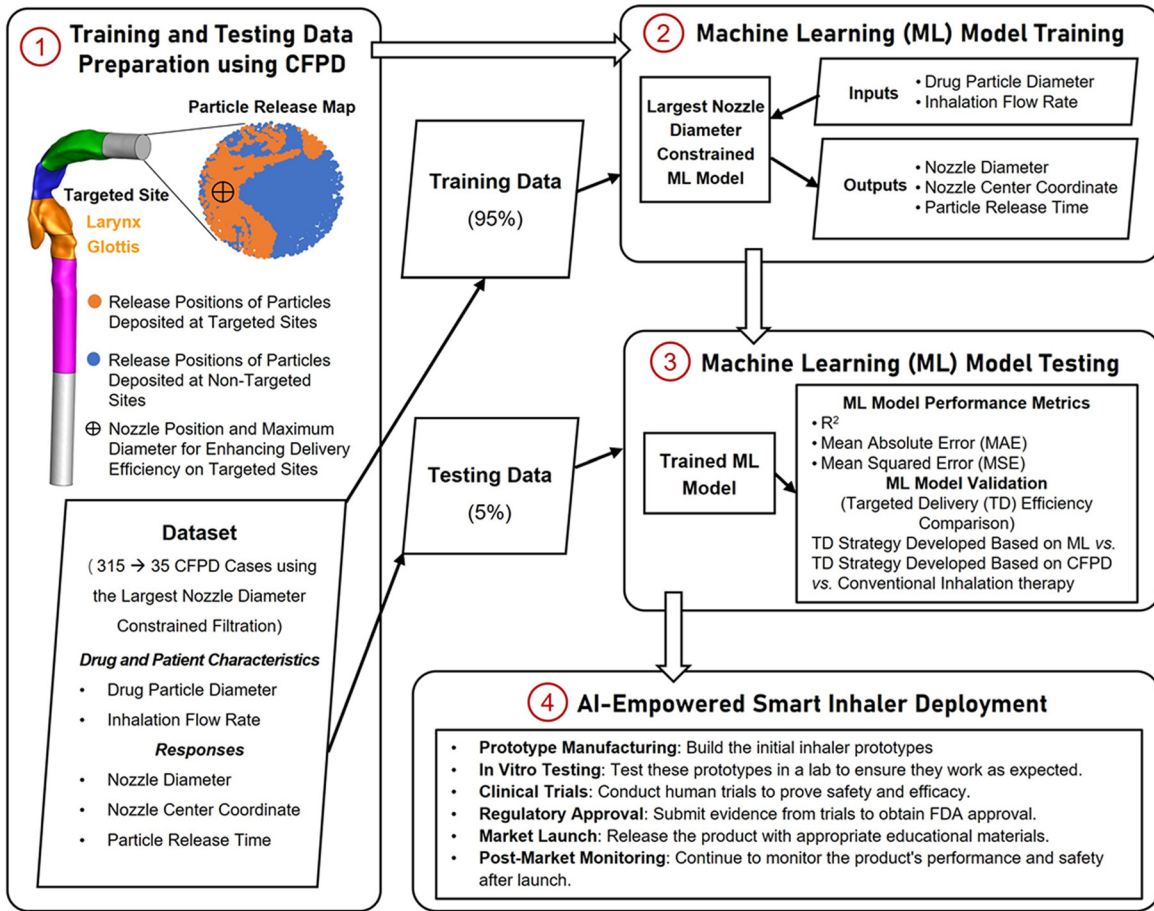
24 February 2024 07:06:57

**FIG. 1.** An illustration of the machine learning (ML) algorithm for achieving the targeted drug delivery from data collection to model training and testing.

in this study, where the total area is 78.54 mm$^2$. The center coordinate of the mouth opening is (x, y, z) = (0, 0, 0) m.

The finite volume mesh was generated using Ansys Fluent Meshing 2022 R1 (Ansys Inc., Canonsburg, PA) and is comprised of unstructured polyhedral mesh elements with near-wall prism layers [see Fig. 3(c)]. Additionally, as shown in Figs. 3(c) and 3(d), 5-layer smooth inflation was generated near the walls to resolve the boundary layer inside the geometry precisely. The mesh independence test was carried out to identify the ultimate mesh with the ideal combination of computational precision and efficiency. The final mesh contains 357 339 cells, 1 710 282 faces, and 1 073 934 nodes. In the mesh independence test described above, the mouth inlet Reynolds number ($Re_{in}$) was set to 8617, corresponding to a peak inhalation flow rate ($Q_{in}$) of 60 l/min at the mouth. This extreme condition was used to validate the robustness of the CFPD model under high flow rates. The mouth inlet velocity of 12.73 m/s was calculated based on the inhalation rate of 60 l/min and the cross-sectional area of the airway at the mouth. The gauge pressure was set to zero at the outlet point, and a non-slip boundary condition was assumed at the airway walls. The mesh independence test was performed using steady-state airflow simulation, assuming the airflow in the airways remains constant over time.

## B. Governing equations

### 1. Computational fluid particle dynamics (CFPD) model

The transition shear-stress transport (SST) model was employed to predict the transitional flow patterns from laminar to turbulence in the geometry from the mouth to the trachea induced by the mouth inlet velocity conditions investigated in this study (see Table I for the inhalation flow rates employed in this study). The governing equations for airflow in tensor form can be given as

$$\frac{\partial u_i}{\partial x_i} = 0, \tag{1}$$

$$\frac{\partial u_i}{\partial t} + u_j \frac{\partial u_i}{\partial x_j} = -\frac{1}{\rho}\frac{\partial p}{\partial x_i} + \frac{1}{\rho}\frac{\partial \tau_{ij}}{\partial x_j} + g_i, \tag{2}$$

in which $\rho$ is the air density, $p$ is the pressure, $u_i$ denotes the air velocity, and $g_i = (9.81, 0, 0)$ m/s$^2$ is the gravitational acceleration. In Eq. (2), the viscous stress tensor $\tau_{ij}$ is defined by

$$\tau_{ij} = \mu \left( \frac{\partial u_i}{\partial x_j} + \frac{\partial u_j}{\partial x_i} \right), \tag{3}$$
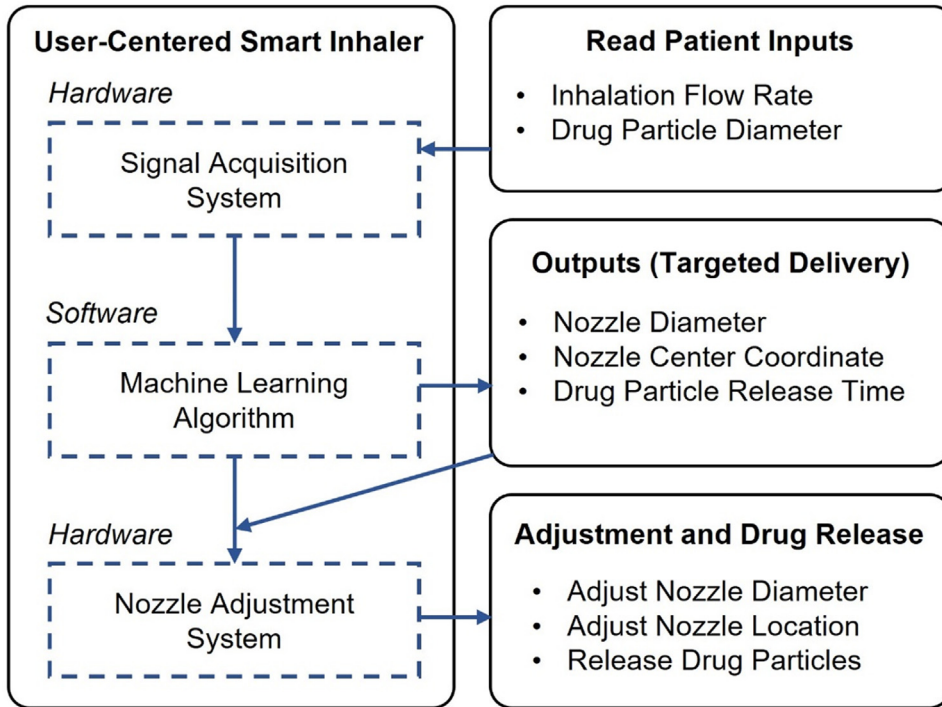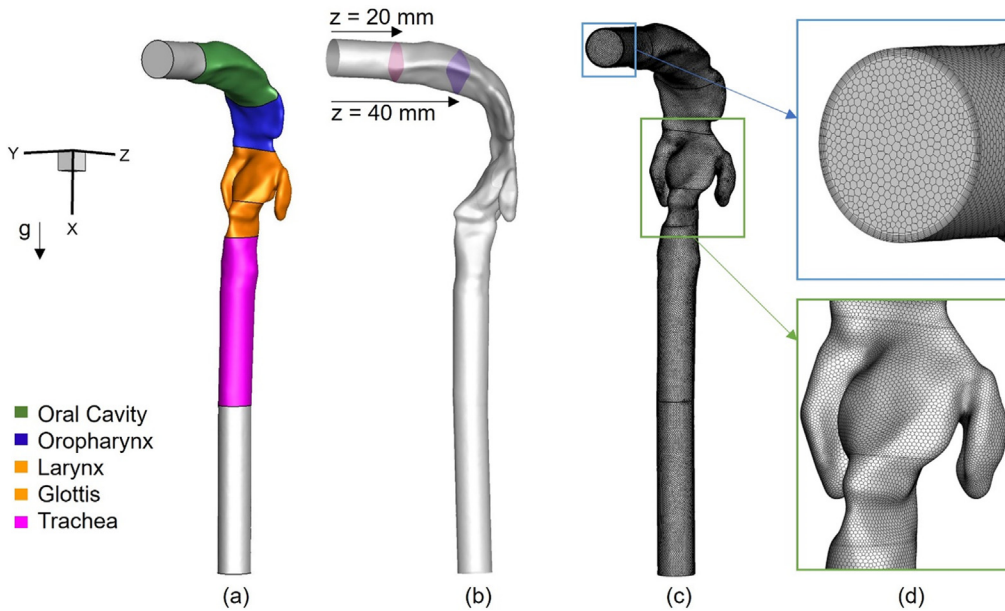
**FIG. 3.** Geometry and mesh details of the 3D mouth-to-trachea airway: (a) Schematic of the mouth opening ($D_{in} = 10$ mm), (b) two particle release positions in the z-direction, (c) polyhedron-based mesh employed in this study, and (d) mesh details at the mouth inlet and larynx–glottis region.

where $\mu$ is the air dynamic viscosity.

This study assumed that the inhaled particles are non-interactive and spherical. The aerodynamic diameter ($d_p$) of inhaled aerosolized particles was from 500 nm to 10 $\mu$m. The study utilized the one-way coupled Euler–Lagrange discrete phase model (DPM) and predicted air-particle transport dynamics in the upper airway.[33] Specifically, it assumes that the particle transport dynamics is affected by the airflow field, but the airflow field remains unchanged by the presence of the

**TABLE I.** Parameter values employed in this study.

| Particle diameter, $d_p$ ($\mu$m) | Inhalation flow rate, $Q_{max}$ (l/min) | Z coordinate of particle release, $z_c$ (m) | Particle release time, $t$(s) |
|---|---|---|---|
| 0.5 | 15 | 0.001 | 0 |
|  | 22.5 |  |  |
| 1 | 30 |  |  |
| 2 | 37.5 | 0.02 | 0.25 |
|  | 45 |  |  |
| 5 |  |  |  |
|  | 52.5 | 0.04 | 0.5 |
| 10 | 60 |  |  |

particles. It was assumed that viscous drag force, Saffman lift force, and gravity were the main forces acting on the particles simulated in this study. The particle translation equation (i.e., Newton's second law) was solved to predict particle trajectories accordingly, i.e.,

$$\frac{d}{dt}\left(m_p\vec{u}_p\right) = \vec{F}_G + \vec{F}_D + \vec{F}_L, \tag{4}$$

where $m_p$ and $\vec{u}_p$ are the mass and velocity of the particle, respectively; $\vec{F}_G$, $\vec{F}_D$, and $\vec{F}_L$ are the gravity, drag force, and Saffman lift force. For particles with $d_p$ larger than 500 nm, the Brownian motion-induced force is negligible. The drag force $\vec{F}_D$ can be given by

$$\vec{F}_D = \frac{1}{8}\pi\rho d_p^2 C_D\left(\vec{u} - \vec{u}_p\right)\left|\vec{u} - \vec{u}_p\right|/C_c, \tag{5}$$

where $d_p$ represents the particle diameter, and $C_c$ stands for the Cunningham correction factor. $C_D$ for spherical particles employed in this study is a function of particle Reynolds number ($Re_p$) and $Re_p$-dependent constants $a_1$, $a_2$ and $a_3$, which can be expressed as[34]

$$C_D = a_1 + \frac{a_2}{Re_p} + \frac{a_3}{Re_p^2}. \tag{6}$$

$Re_p$ can be defined as[35]

$$Re_p = \frac{\rho\left|\vec{u} - \vec{u}_p\right|d_p}{\mu}. \tag{7}$$

In Eq. (5), the Cunningham correction factor $C_c$ can be given by[36]

$$C_c = 1 + \frac{2\lambda}{d_p}\left(1.257 + 0.4e^{-0.55\frac{d_p}{\lambda}}\right), \tag{8}$$

in which $\lambda$ is the mean free path of air.

The Saffman lift force $\vec{F}_L$ is particularly noticeable for particles with large size.[37] The tensor form $F_{L,i}$ can be given by[38]

$$F_{L,i} = m_p\frac{2K\nu^{0.5}d_{ij}}{Sd_p(d_{lk}d_{kl})^{\frac{1}{4}}}\left(u_j - u_j^p\right), \tag{9}$$

where $K = 2.594$ is the constant coefficient of Saffman lift force, $\nu$ is kinematic viscosity, $S$ is the ratio of particle density to fluid density, and $d_{ij}$ is the deformation rate, which is

$$d_{ij} = \frac{1}{2}\left(u_{i,j} + u_{j,i}\right). \tag{10}$$

It is worth noting that the CFPD model employed in this study has been extensively validated by the comparisons with benchmark experimental data on pulmonary airflow field and particle deposition, which can be found in previous publications.[39–42]

### 2. Machine learning (ML) algorithm

As a part of data preparation for ML model, a total of 315 CFPD simulations were conducted depending on the variables used, i.e., peak inhalation flow rate ($Q_{max}$) and particle aerodynamic diameter ($d_p$) (see Table I) to find the optimal nozzle diameter ($D_{nozzle}$) and nozzle location ($x_c, y_c, z_c$) to maximize drug deposition in the diseased site (i.e., larynx and glottis). $Q_{max}$ and $d_p$ are patient-specific and medication-specific information depending on the prescription and patient–inhaler coordination, which were selected as ML model inputs. However, each pair of inhalation flow rate and particle diameter has nine related CFPD simulations, and the differences were based on varying particle release time and z-coordinate. To keep a one-to-one mapping for ML model, one simulation case needed to select from each of nine CFPD cases simulated from each of inhalation flow rate and particle diameter pair. The selection criteria were to find the CFPD result, which has the maximum available nozzle diameter for targeted delivery from the mentioned nine CFPD case groups. Hence, the ML model dataset was reduced to only samples as training and testing data. Due to the limitations of the samples for the training and testing data, 95% of the data were used for the training set. The complete training and testing dataset is provided in Appendix A in the supplementary material.

Several ML multi-output regression models were employed initially to optimize nozzle position and nozzle diameter for more effective targeted delivery to larynx and glottis with aerosolized particles, based on the patient-specific input parameters mentioned in Fig. 1. The ML regression models employed as candidates for comparison in this study include support vector machine (SVM), random forest (RF), Gaussian process regression (GPR), and decision tree (DT) [i.e., classification and regression trees (CART)].[43,44] The objective of applying multiple models was to find which one performs the best with this specific smart inhaler CFPD simulation data. Through comparison, the CART regression model was selected based on the evaluation metrics using different ML models listed in Table II.

Specifically, to evaluate the performances of ML models employed on the smart inhaler data set, three evaluation metrics were used, i.e., mean squared error (MSE), mean absolute error (MAE), and coefficient of determination ($R^2$). ML models were trained and tested based on the two inputs (i.e., drug particle diameter and inhalation flow rate) and five outputs (i.e., nozzle center Cartesian coordinates, nozzle diameter, and particle release time). Accordingly, the evaluation metrics need to be defined for a multioutput regression problem. Thus, the metrics were defined as

$$MSE = \frac{1}{mn}\sum_{i=1}^{m}\sum_{j=1}^{n}\left(y_{ij} - \hat{y}_{ij}\right)^2, \tag{11}$$

$$MAE = \frac{1}{mn}\sum_{i=1}^{m}\sum_{j=1}^{n}\left|y_{ij} - \hat{y}_{ij}\right|, \tag{12}$$

**TABLE II.** ML model accuracy for training and testing data for multiple ML models used. Note: * indicates the best model compared to the other ML model without further improvements. The DT* model then further optimized using GridSearchCV technique for multiple K-fold values (see Table VII).

| | Training size = 0.70 and KFold = 5 | | | | | | | |
| --- | --- | --- | --- | --- | --- | --- | --- | --- |
| | SVM | | RF | | GPR | | DT | |
| | For training data | For testing data | For training data | For testing data | For training data | For testing data | For training data | For testing data |
| MSE | 0.5801 | 0.0722 | 0.0015 | 0.0022 | 0.4487 | 0.0962 | 0.0015 | 0.0028 |
| MAE | 0.4809 | 0.1661 | 0.0139 | 0.0164 | 0.5359 | 0.1684 | 0.0136 | 0.0161 |
| $R^2$ | 0.4199 | −263.0 | 0.5848 | 0.0611 | 0.5513 | −55 591.0 | 0.6003 | 0.1975 |
| | Training size = 0.95 and KFold = 5 | | | | | | | |
| | SVM | | RF | | GPR | | DT* | |
| | For training data | For testing data | For training data | For testing data | For training data | For testing data | For training data | For testing data |
| MSE | 0.6023 | 0.0784 | 0.0017 | 0.0002 | 0.6538 | 0.1109 | 0.0014 | 0.0001 |
| MAE | 0.4807 | 0.1773 | 0.0161 | 0.0090 | 0.5994 | 0.2721 | 0.0130 | 0.0029 |
| $R^2$ | 0.3977 | −92.02 | 0.4993 | −0.0038 | 0.3462 | −58 278.0 | 0.5057 | 0.6545 |

$$R^2 = 1 - \frac{\sum_{i=1}^{m}\sum_{j=1}^{n}\left(y_{ij} - \hat{y}_{ij}\right)^2}{\sum_{i=1}^{m}\sum_{j=1}^{n}\left(y_{ij} - \bar{y}_i\right)^2}, \qquad (13)$$

where $\hat{y}_{ij} = (\hat{x}_{cj}, \hat{y}_{cj}, \hat{z}_{cj}, \hat{t}_j, \hat{D}_{nozzle,j})$ is the predicted value of the dependent variable $i$ for each data point $j$, $y_{ij} = (x_{cj}, y_{cj}, z_{cj}, t_j, D_{nozzle,j})$ is the actual value of the dependent variable $i$ for each data point $j$, $\bar{y}_i = (\bar{x}_{cj}, \bar{y}_{cj}, \bar{z}_{cj}, \bar{t}_j, \bar{D}_{nozzle,j})$ is the mean of all the actual values for output $i$ across all data points, $m$ is the number of outputs, and $n$ is the total number of sample data. $D_{nozzle}$ is the maximum (optimal) nozzle diameter for targeted delivery, $t$ is the particle release time, and $(x_c, y_c, z_c)$ are the center coordinates of the nozzle drug delivering position.

Table II displays the performance of multiple ML models trained and tested in this study, conducted with varying training dataset sizes and employing a K-fold cross-validation approach with a value of 5. These evaluations were carried out before any additional model optimizations were applied. With a training size is 0.70, both SVM and GPR exhibit poor $R^2$ values, while RF and DT model shows decent $R^2$ results. However, as the training size increases to 0.95, the $R^2$ value for the DT model improves along with reductions in both MSE and MAE. This indicates that the DT model (i.e., CART) is more suitable for the smart inhaler dataset. Therefore, DT model has been selected and optimized further for this study.[44] It is also worth mentioning that the DT model can also be directly visualized with good interpretability. A more comprehensive description of the CART model employed in this study can be found in Appendix B in the supplementary material.

The optimized CART tree is trained and tested using the CFPD dataset and then evaluated based on the metrics defined in Eqs. (6)–(8). To further evaluate the prediction performances of the ML model, DFs predicted using ML based targeted delivery strategy were compared with the DFs using both conventional inhalation therapy

and targeted delivery strategy based on CFPD. Two threshold values were defined to find the success rate of the CART model on targeted delivery. More details on the ML model success criteria are explained in Sec. III B 2.

## C. Initial and boundary conditions

To create the training and testing dataset, a parametric analysis is performed to evaluate the effects of different factors on the targeted drug delivery using the proposed user-centered smart inhaler. A total of 315 CFPD simulations were conducted to generate the data. CFPD simulation results and post-processed data are recorded as samples for training and testing dataset. Figure 1 shows the details of the training and testing data structure. To achieve informative and reliable outcomes regarding the objectives, the CFPD simulations and analysis explored the impact of particle diameter, inhalation flow rates, particle release time, and particle release position on drug delivery efficiency to larynx and glottis. More details on the parametric study with different initial and boundary conditions can be found in Table I.

### 1. Mouth inlet condition

Idealized sinusoidal airflow velocity profiles with an inhalation to exhalation time duration ratio of 1:1 were used to represent the airflow inlet conditions at the mouth opening.[45] For this study, seven different flow rates are considered (see Table I). The corresponding average mouth inlet velocity varied between 3.18 and 12.73 m/s. Figure 4 shows all breathing waveforms. The transient inhalation–exhalation flow rate $Q$ is defined as follows:

$$Q_{in} = Q_{max}\sin\left(\frac{2\pi t}{T}\right). \qquad (14)$$

Here, $Q_{max}$ refers to the maximum flow rate, and $T$ represents the total inhalation–exhalation time, which has been set to 2 s. The peak
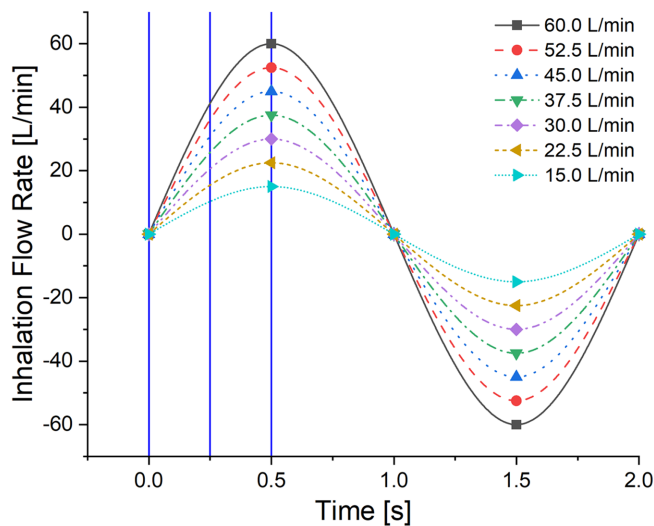
**FIG. 4.** Sinusoidal inhalation–exhalation waveform with seven peak inhalation flow rates. Note: Blue vertical lines indicate particle release times (t = 0.0, 0.25, and 0.5 s).

inhalation flow rates employed in this study are 15, 22.5, 30, 37.5, 45, 52.5, and 60 l/min.

A total of 11 330 spherical particles with density of 1000 kg/m³ were injected through the mouth inlet in the positive z direction (see Fig. 3). Particle number independence test has been carried out to find the optimum number of particles considering the best balance between computational accuracy and time (see the Appendix C in the supplementary material).

### 2. Airway wall boundary condition

No-slip wall boundary condition is applied on airway walls. For particle deposition, the simulation model includes a "trap" boundary condition at the wall of the respiratory tract, due to the presence of mucus layers inside the airway. Because of the trap boundary condition, the coefficient of restitution is equal to zero, resulting in no particle reflections when the distance between the particle center and the airway wall is less than the particle radius.

### 3. Trachea outlet condition

Gauge pressure was set to zero at the trachea outlet, while an "escape" condition is considered at both mouth inlet and trachea outlet. Physiologically, the escape condition implies that the particles leaving the trachea outlet and may deposit somewhere in tracheobronchial tree.

### D. Numerical setup

To predict the transport and deposition of inhaled aerosolized medication particles to larynx and glottis to treat JORRP patient, back-track particles, generate particle release maps, and prepare the training and testing dataset, Ansys Fluent 2022 R1 (Ansys Inc., Canonsburg, PA) was employed. To maintain numerical stability, a time step of 0.01 s was employed for the flow and the simulation was regarded as

fully converged when all residuals dropped below $10^{-4}$. The Navier–Stokes (N–S) equations were resolved using a second-order upwind momentum simple scheme and pressure–velocity coupling method in both space and time using the finite-volume method. The Dell Precision T7910 workstation that has an Intel® Xeon® Processor E5-2643 v4 with dual processors, 64 cores, and 128 GB RAM was used for the numerical simulations. Each simulation took approximately 3 h using six threads to complete with a 2 s inhalation–exhalation cycle (see Fig. 4).

In-house user-defined functions (UDFs), MATLAB, and Python codes were used for:

(1) Generating the monodispersed drug particles injection files;
(2) Specifying the transient sinusoidal inhalation waveform at the mouth opening;
(3) Setting the DPM drag coefficient;
(4) Defining the DPM time step;
(5) Generating results for particle deposition data in the respiratory route of the lung through post-processing; and
(6) Finding the maximum diameter of the inscribed circle as the optimal nozzle diameter for particle release to achieve targeted delivery to larynx and glottis.

## III. RESULTS AND DISCUSSION
### A. CFPD results
#### 1. Airflow field in upper airway

Figures 5–7 show the airflow velocity magnitude contours and the secondary flow velocity vectors across seven representative cross sections (AA′ to GG′) within the airway geometry for three representative time peak inhalation flow rate $Q_{max}$, i.e., 15, 37.5, and 60 l/min. All the contours were generated at the flow time of t = 0.5 s, which are at the peak inhalation flow and $z_c = 0.001$ m. It can be observed that the airflow velocity distributions in each cross section have no noticeable variations with the increase in inhalation flow rate despite the changes in velocity magnitude (see Figs. 5–7). One vortex can be observed at DD′, which is located at larynx. Furthermore, relatively higher velocities and skewed velocity distributions can be found in the DD′ and EE′, which are due to the reduction in lumen in larynx and glottis, as well as the formation of laryngeal jet core because of the inertial impaction of inhaled airflows (see iso-surfaces shown in Figs. 5–7). Figures 5–7 also illustrate the 3D iso-surfaces of velocity magnitude highlighting the structure of the laryngeal jet. It can be observed that in all laryngeal jet cores (see Figs. 5–7), a high-velocity stream is generated as the airflow transits through the glottis with the contraction before entering the trachea. It is worth noting that the tracheal jet is not aligned with the axial centerline of the trachea, due to the inertial effect of the inhaled airflow after impinging the pharynx.

#### 2. Local particle deposition

To investigate the impact of $Q_{max}$ and $d_p$ on local particle deposition patterns from mouth to trachea, three representative particle sizes (i.e., $d_p$ = 500 nm, 2, and 10 $\mu$m) were selected for comparison at peak inhalation flow rate $Q_{max}$ from 15 to 60 l/min, as shown in Figs. 8–10. For cases shown in Figs. 8–10, the particle release time and the particle release z-position maintained constant at t = 0.0 s and $z_c = 0.001$ m, respectively.
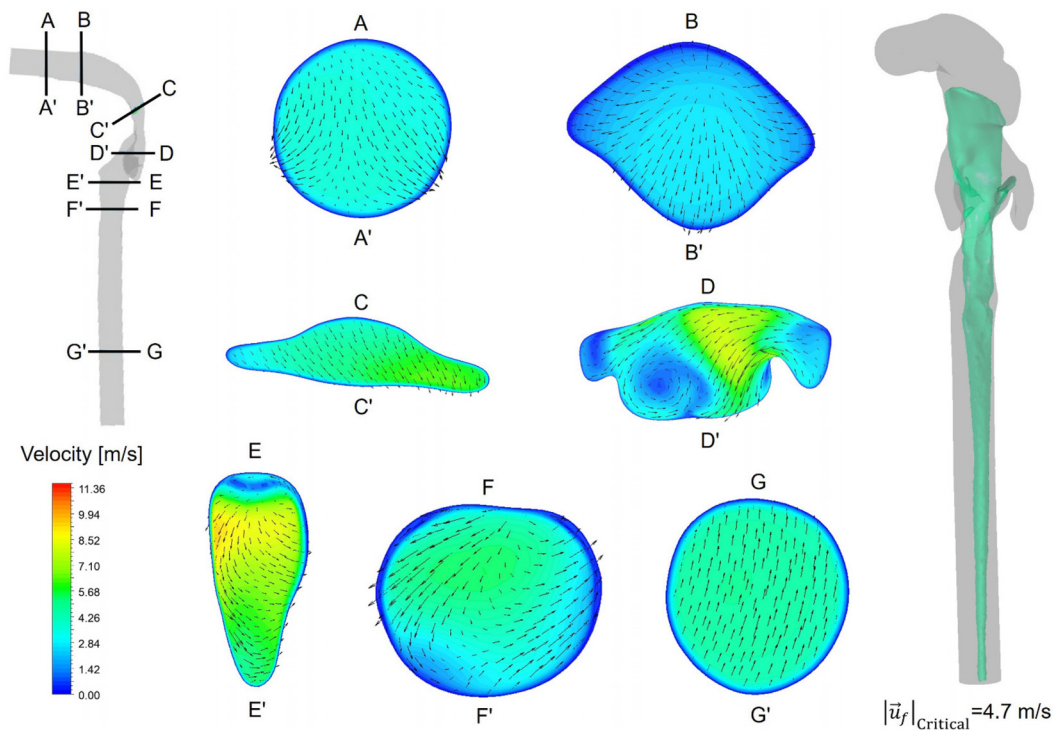
**FIG. 5.** Velocity contours at multiple cross sections and laryngeal jet core (critical velocity for iso-surface generation $|\vec{u}_f|_{\text{Critical}} = 4.7$ m/s) with a peak inhalation flow rate of 15 l/min.

Specifically, Figs. 8(a)–8(g) show local particle deposition patterns for the smallest particles (i.e., $d_p = 500$ nm) used in this study, aiming to investigate how local particle deposition varies with $Q_{\max}$. It can be observed from Figs. 8(a)–8(g) that very few particles deposited in the oral cavity and oropharynx despite the changes in $Q_{\max}$ with 500 nm particles. At the lowest $Q_{\max}$ of 15 l/min, most particles exited the trachea outlet with only a few particles deposited in the trachea region [see Fig. 8(a)]. As the $Q_{\max}$ increased from 15 to 60 l/min, more particles deposited from the larynx to trachea [see Figs. 8(b)–8(g)], which is mainly due to the enhanced turbulence dispersion effect. Accordingly, 500 nm particles started to deposit in the larynx to trachea region with the increasing $Q_{\max}$. Furthermore, Figs. 8(d)–8(g) show that when $Q_{\max}$ increased from 37.5 to 60 l/min flow rate, total depositions of 500 nm particles increased and the regional deposition also increased in the larynx to trachea region. Meanwhile, there were still a considerable number of particles leaving the trachea and entering the tracheobronchial (TB) tree. Such a finding indicates that to achieve targeted drug delivery to the larynx and glottis region is necessary since it will avoid particle deposition in TB tree to cause side effects.

Figures 9(a)–9(g) illustrate local particle deposition patterns for 2 $\mu$m particles at different $Q_{\max}$. These figures explain very similar trends between local particle deposition patterns and the variation of $Q_{\max}$ like 500 nm particles [see Figs. 8(a)–8(g)], with very few particles depositing in the oral cavity and oropharynx area, and a huge number of particles exiting the trachea, even with the increased inhalation flow rate. Also, the deposition in the larynx to trachea part is less with lower

$Q_{\max}$, as shown in Figs. 9(a)–9(c). Following the same trend, the deposition increases with the increasing flow rate [see Figs. 9(d)–9(g)]. The maximum deposition can be found at $Q_{\max} = 60$ l/min flow rate for 2 $\mu$m particles, whereas the lowest deposition was seen for 15 l/min. One noticeable difference between the deposition of 500 nm and 2 $\mu$m particles is that there is more particle deposition in the mouth-to-trachea region for the 500 nm particles, which is possibly due to the higher turbulence dispersion effect with smaller particle size.

The local deposition patterns for 10 $\mu$m particles are presented in Figs. 10(a)–10(g). Due to the stronger inertial impaction effect of these larger size particles, most of the particles deposited at the back of the oral cavity and pharynx, with significantly fewer particles deposited in larynx and glottis and nearly no particles deposited in the trachea. In addition, with a relatively low $Q_{\max}$, 10 $\mu$m particles deposited more in the larynx and trachea region, spanning from the oral cavity to larynx region [see Figs. 10(a)–10(c)]. In contrast, at higher flow rates ($Q_{\max} \geq 37.5$ L/min), almost all particles deposited in the oral cavity to oropharynx region and only a few particles deposited on larynx [see Figs. 10(d)–10(g)]. For $Q_{\max} = 52.5$ and 60 l/min, particles deposited in the oral cavity and oropharynx regions [see Figs. 10(f)–10(g)]. This is because increasing inhalation flow rate will increase the particle inertial impaction effect, which leads to more particles depositing in the oral cavity and back of the pharynx with the stronger impingement of the airflow. One noticeable difference for 10 $\mu$m particle local deposition is that all the injected particles deposited before leaving the larynx and glottis area, whereas a substantial number of the 500 nm and
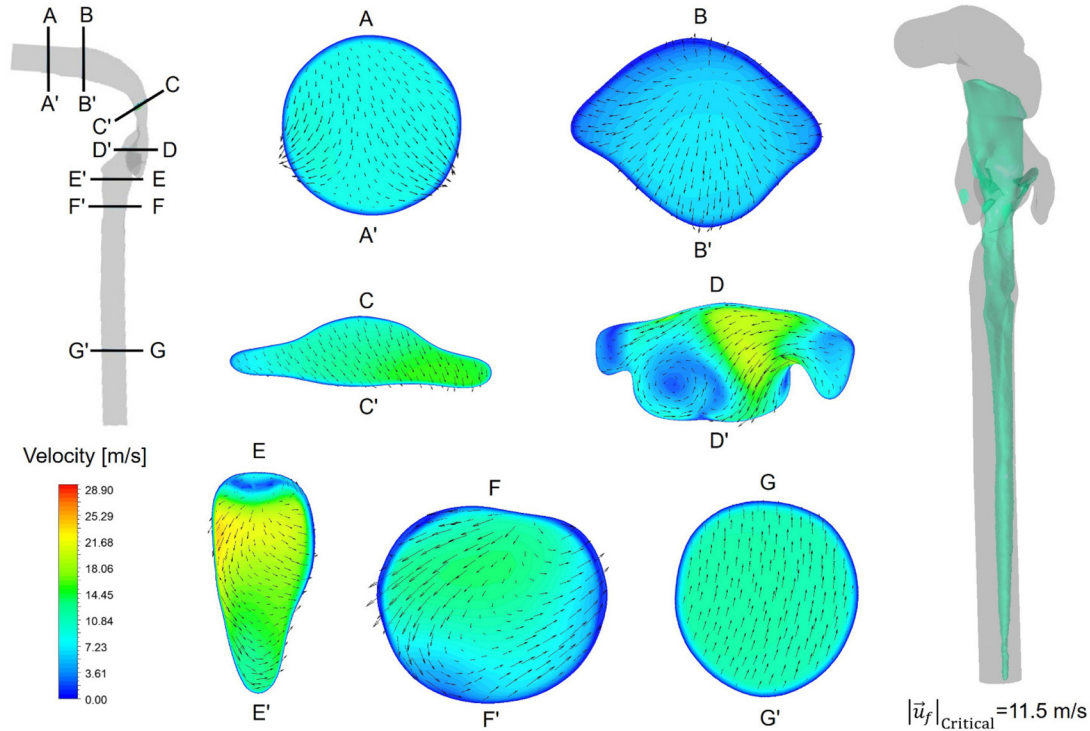
**FIG. 6.** Velocity contours at multiple cross sections and laryngeal jet core (critical velocity for iso-surface generation $|\vec{u}_f|_{\text{Critical}} = 11.5$ m/s) with a peak inhalation flow rate of 37.5 l/min.

10 $\mu$m particles can exit the trachea. This indicates that using large particle size may reduce the potential for them entering TB tree to cause side effects.

### 3. Optimal Nozzle Diameter and Location vs $Q_{max}$ and Particle Release Time

To investigate the impact of the peak inhalation flow rate and particle release time on the available nozzle diameter for particle release to achieve targeted delivery, 12 representative particle release maps are visualized in Fig. 11 associated with multiple $Q_{max}$ and the particle release times. Simulations were conducted with 10 $\mu$m particles, using $Q_{max} = 15$, 22.5, 30, 37.5, 45, 52.5, and 60 l/min and three particle release times t = 0.0, t = 0.5, and t = 1.0 s. Based on the full-mouth drug release CFPD simulation results (i.e., conventional inhalation therapy simulations), the particle release maps shown in Fig. 11 were generated using the backtracking strategy where the precise particle release coordinates were colored by their deposition sites in the airway. Specifically, particles were colored orange if they deposited at the pharynx or glottis region, while blue particles deposited at other locations in the upper airway. Therefore, using the particle release maps can predetermine the available region for particle release to deliver the medications to the targeted regions, i.e., pharynx and glottis to treat JORRP. Another purpose of using particle release maps is to identify the maximum nozzle diameter and optimal location for precise particle release for targeted drug delivery. An in-house Python code was used

to find the optimal position and diameter of the nozzle in the available, orange-colored area in the particle release maps to maximize the targeted drug delivery. The black-colored dotted circle in Fig. 11 shows the maximum diameter and the location of the nozzle. The corresponding nozzle diameters and positions for all the flow rates and particle release time used for the targeted delivery are also tabulated in Table III. The deposition fractions (DF) of those conventional inhalation therapies from the CFPD simulation results are presented in Table III as well.

The particle release maps displayed in Fig. 11 highlight the significant impact of both particle release time and peak inhalation flow rates on determining the optimal nozzle diameter $D_{\text{nozzle}}$ and location $(x_c, y_c, z_c)$ for targeted drug delivery to the pharynx and glottis. However, this influence does not follow a straightforward or linear pattern. Specifically, when the peak inhalation flow rate $Q_{max}$ is set at 15 and 30 l/min, an increase in nozzle diameter can be observed as the particle release time increases from t = 0.0 to t = 0.5 s. In contrast, at 45 and 60 l/min, the CFPD results presented in Fig. 11 reveal that the nozzle diameter decreases as the best release time extends from t = 0.0 to t = 0.5 s. Furthermore, while the optimal nozzle location does vary with changes in both inhalation flow rate and particle release time, there is also no clear-cut, monotonic relationship between these parameters and nozzle locations. This complex and non-linear relationship between parameters and nozzle diameter $D_{\text{nozzle}}$ and location $(x_c, y_c, z_c)$, necessary for precise targeted delivery, underscores the need to employ ML and/or deep learning (DL)
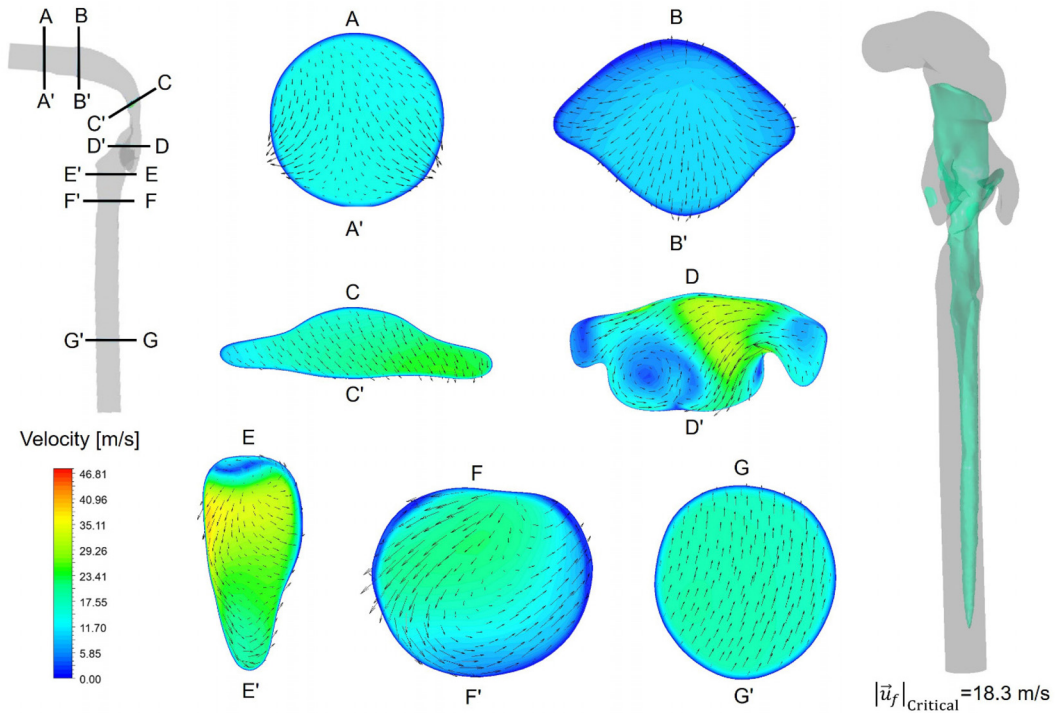
**FIG. 7.** Velocity contours at multiple cross sections and laryngeal jet core (critical velocity for iso-surface generation $|\vec{u}_f|_{\text{Critical}} = 18.3$ m/s) with a peak inhalation flow rate of 60 l/min.

methodologies to comprehensively study and predict these intricate relationships.

It is also worth mentioning that one difference was observed in the release map for 15 l/min flow rate and t = 0.25 s release time in Fig. 11. This particle release map has a big, orange-colored available region for targeted delivery, which can also be supported by the relatively high DF of 80.38% from Table III. However, several blue-colored particles, which are not depositing in non-targeted region, are
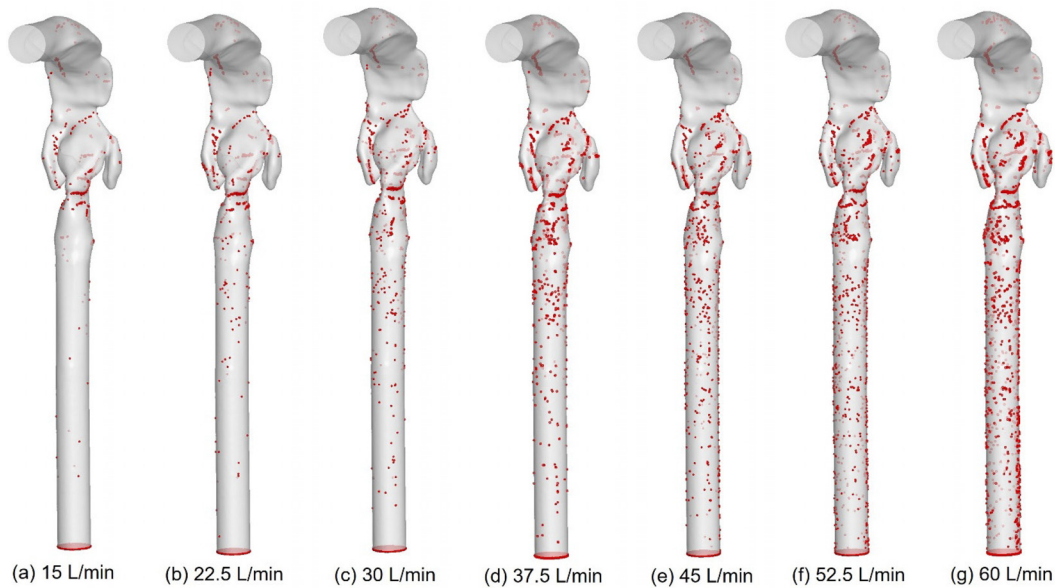


**FIG. 8.** Local deposition patterns of inhaled particles ($d_p = 500$ nm) at release time t = 0.0 s with multiple peak inhalation flow rates.

**FIG. 9.** Local deposition patterns of inhaled particles ($d_p = 2\ \mu$m) at release time t = 0.0 s with multiple peak inhalation flow rates.



**FIG. 10.** Local deposition patterns of inhaled particles ($d_p = 10\ \mu$m) at release time t = 0.0 s with multiple peak inhalation flow rates.
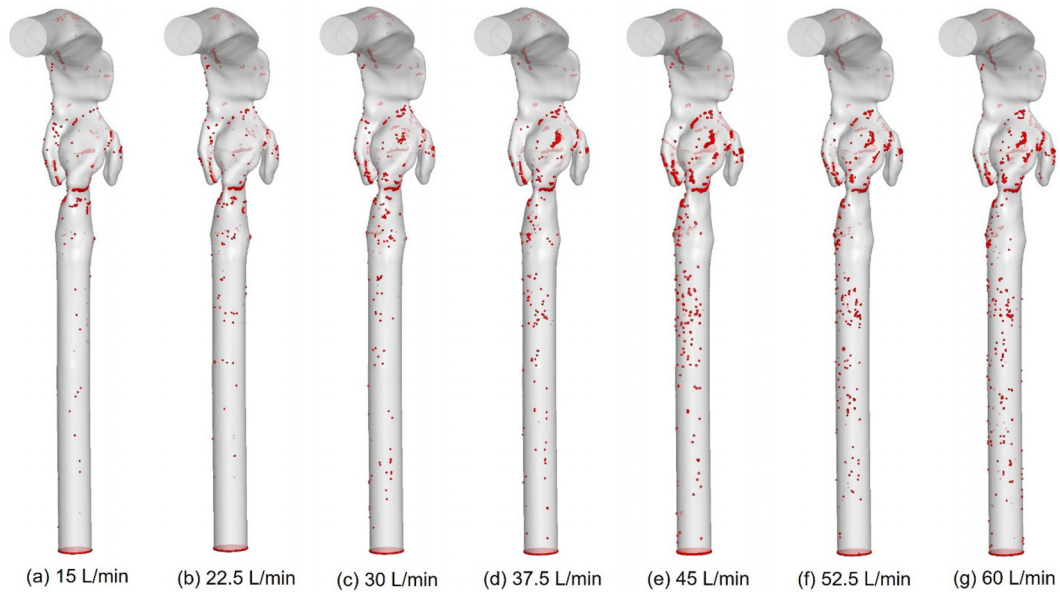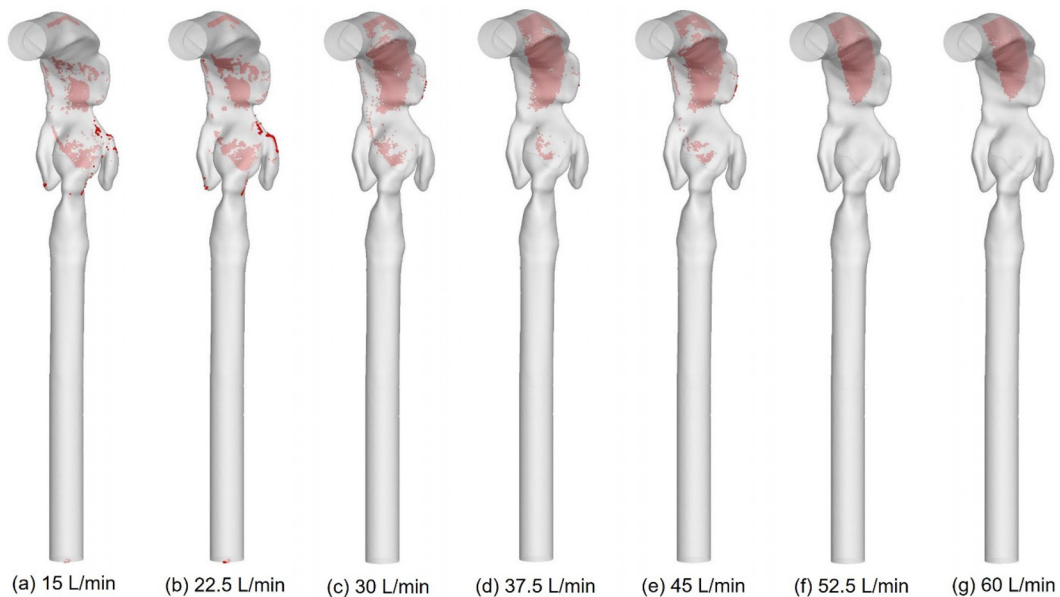
trapped in the inscribed orange region. It is the reason that the optimal nozzle diameter kept smaller even the release map seems have a bigger available targeted region.

Another noticeable finding is that when the particles are injected at t = 0.0 s, the nozzle diameter increases with the increase in $Q_{max}$.

However, opposite trends between nozzle diameter and $Q_{max}$ are shown for release time t = 0.25 and t = 0.5 s, in which the nozzle diameters are decreasing or remaining almost similar when $Q_{max}$ increased. Since both inhalation flow rate and particle release time can influence the inlet Reynolds number ($Re_{in}$) at the time of drug particle release,
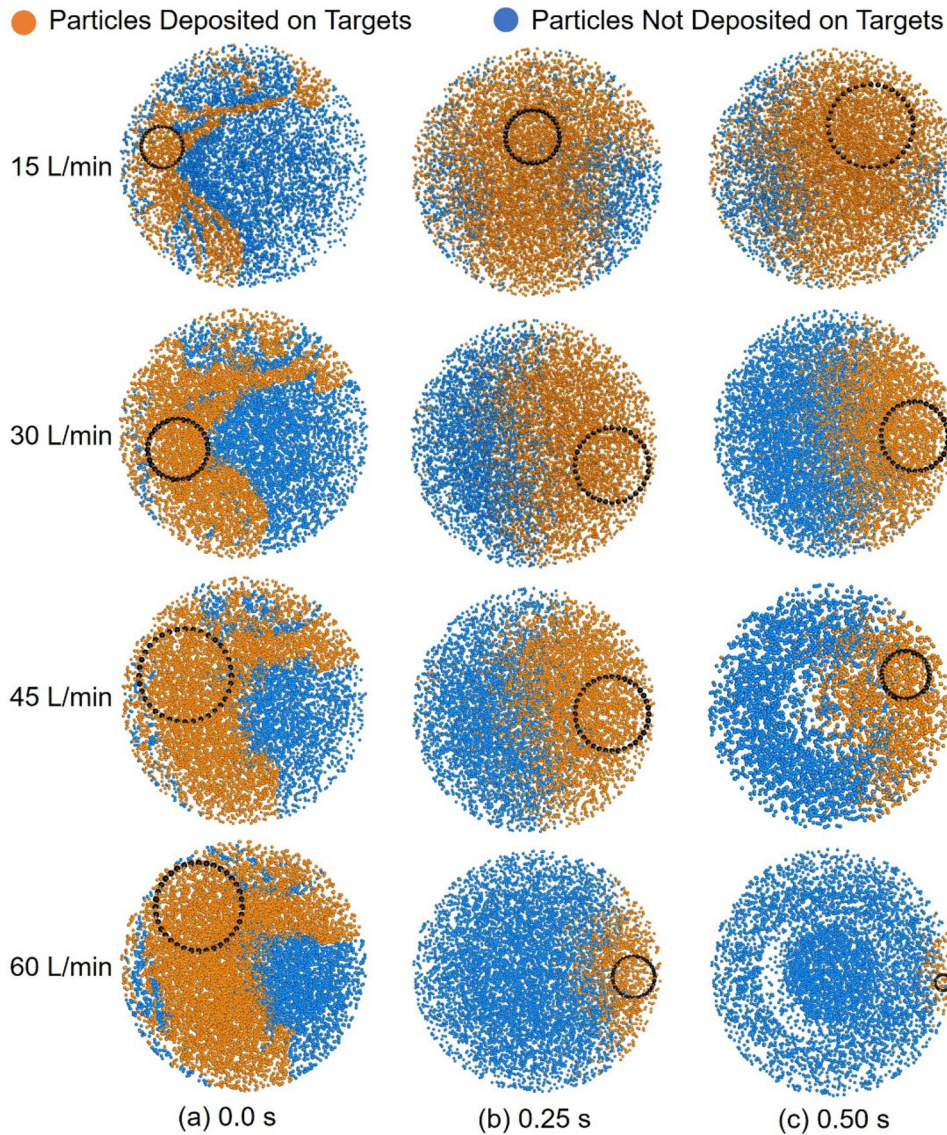
**FIG. 11.** Particle release maps at three different particle release time with four different peak inhalation flow rates for particles with $d_p = 10\ \mu m$ and z-coordinate of particle release position at $z_c = 0.001$ m.

additional figures (see Figs. 12–14) are presented to show the data trends between the optimal $x_c$ and $y_c$ coordinates of the nozzle center, the optimal nozzle diameter $D_{nozzle}$, and $Re_{in}$ at the time of particle release. The purpose of analyzing Figs. 12–14 is to investigate whether there are clear relationships that can be shown between ML inputs and outputs (see Fig. 1).

Specifically, Figs. 12(a)–12(c) highlight the relationship between the optimal nozzle center $x_c$ coordinate and $Re_{in}$ across multiple $z_c$ coordinates of the nozzle center for particle release (i.e., $z_c = 0.001$, 0.02, and 0.04 m). Concurrently, Fig. 12(d) provides 95% confidence ellipses for the three datasets shown in Figs. 12(a)–12(c). It can be observed from Figs. 12(a)–12(c) that there are no clear trends of optimal nozzle x coordinates with the increase in $Re_{in}$ across all three nozzle $z_c$ release coordinates. Nonetheless, a subtle increase in the optimal

nozzle x coordinate with $Re_{in}$ is faintly discernible through the confidence ellipses in Fig. 12(d), although the impact of the nozzle center $z_c$ coordinate on the optimal nozzle $x_c$ coordinate appears to be negligible. Meanwhile, Figs. 13(a)–13(c) elucidate the relationship between the optimal nozzle center y coordinate and $Re_{in}$ at particle release across the same multiple $z_c$ coordinates of the nozzle center as investigated in Figs. 12(a)–12(c). Figure 13(d) showcases 95% confidence ellipses for the three datasets presented in Figs. 13(a)–13(c). Similar to the observations in Fig. 12, there is no distinct pattern in the optimal nozzle $y_c$ coordinates with the escalation in $Re_{in}$ for all three nozzle $z_c$ release coordinates shown in Figs. 13(a)–13(c). From the confidence ellipses presented in Fig. 13(d), it can be observed, the optimal nozzle $y_c$ coordinate decreases when particles are released deeper within the mouth (i.e., at larger $z_c$ coordinates). Figures 14(a)–14(d) further suggest that

**TABLE III.** Corresponding nozzle diameter and deposition fraction at three different particle release time with three different flow rates for 10-$\mu$m particle injection.

| Peak inhalation flow rate, $Q_{max}$ (l/min) | Particle release time, t (s) | Nozzle Z-coordinate, $z_c$ (m) | Nozzle X-coordinate, $x_c$ (m) | Nozzle Y-coordinate, $y_c$ (m) | Nozzle diameter, $D_{\text{Nozzle}}$ (m) | Deposition fraction (DF) (%) |
|---|---|---|---|---|---|---|
| 15 | 0.0 | 0.001 | −0.003 295 | 0.000 786 | 0.001 702 | 24.87 |
| 15 | 0.25 | 0.001 | −0.000 179 | 0.001 452 | 0.002 170 | 80.38 |
| 15 | 0.5 | 0.001 | 0.001 514 | 0.001 809 | 0.003 431 | 82.52 |
| 30 | 0.0 | 0.001 | −0.002 634 | −0.000 649 | 0.002 435 | 53.69 |
| 30 | 0.25 | 0.001 | 0.003 184 | −0.000 840 | 0.003 015 | 62.83 |
| 30 | 0.5 | 0.001 | 0.003 387 | −0.000 122 | 0.002 813 | 41.98 |
| 45 | 0.0 | 0.001 | −0.002 417 | 0.001 023 | 0.003 782 | 62.17 |
| 45 | 0.25 | 0.001 | 0.003 242 | −0.000 155 | 0.003 046 | 52.54 |
| 45 | 0.5 | 0.001 | 0.002 504 | −0.000 124 | 0.003 287 | 27.78 |



**FIG. 12.** Optimal nozzle x coordinates vs mouth inlet $Re_{in}$ at particle release time: (a) Optimal nozzle x coordinate vs $Re_{in}$ for particle release z-coordinate $z_c = 0.001$ m, (b) optimal nozzle x coordinate vs $Re_{in}$ for particle release z-coordinate $z_c = 0.02$ m, (c) optimal nozzle x coordinate vs $Re_{in}$ for particle release z-coordinate $z_c = 0.04$ m, and (d) confidence ellipses for data shown in (a), (b), and (c).
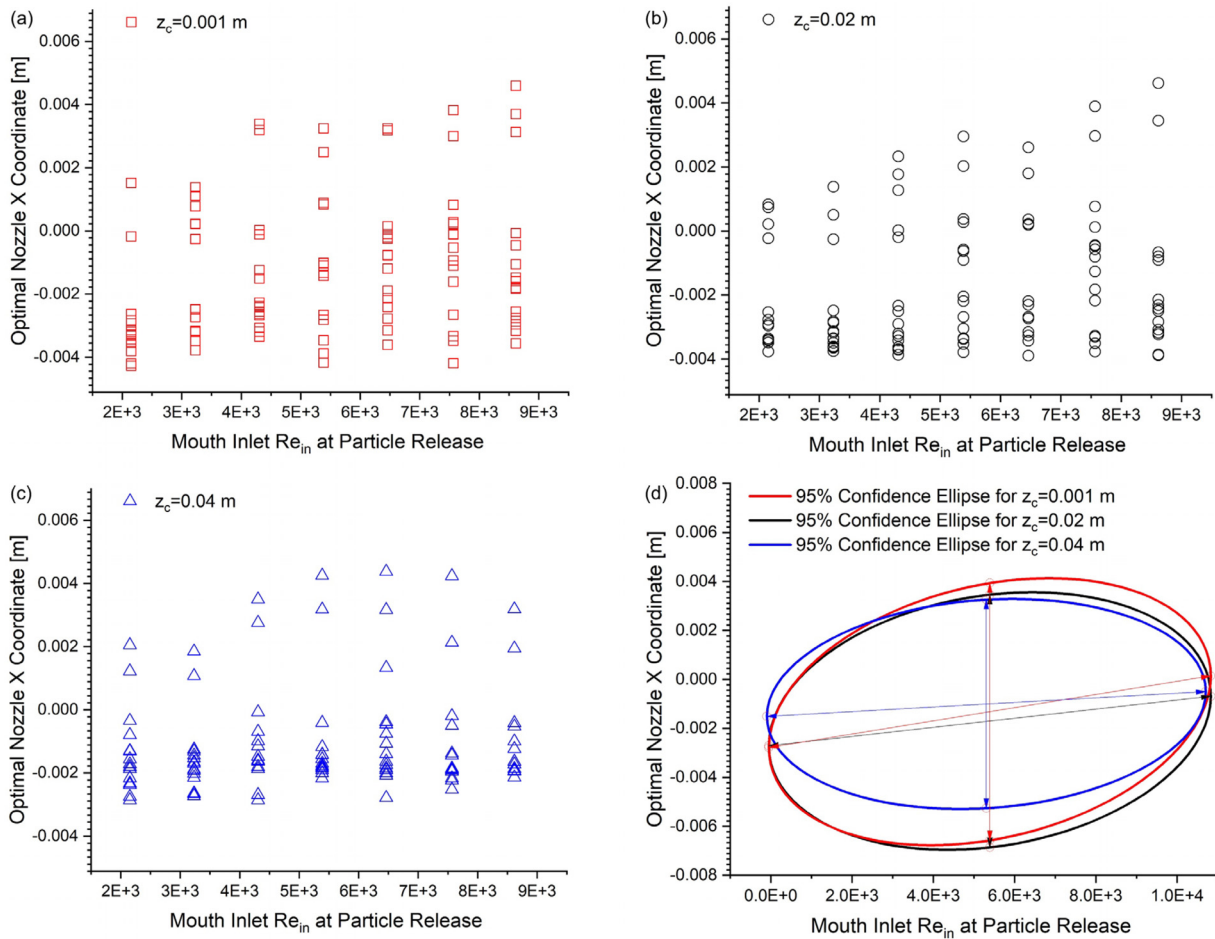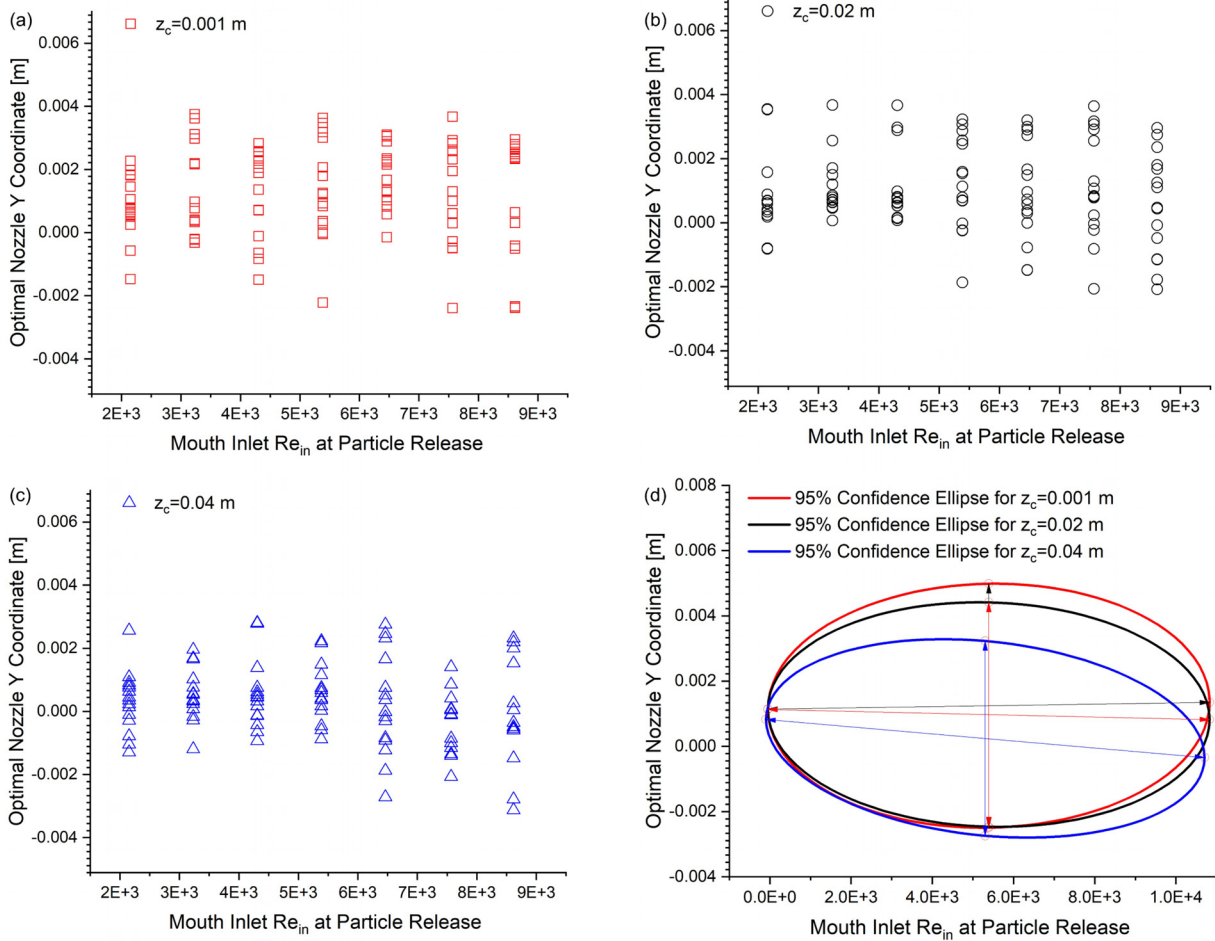
**FIG. 13.** Optimal nozzle y coordinates vs mouth inlet $Re_{in}$ at particle release time: (a) Optimal nozzle y coordinate vs $Re_{in}$ for particle release z-coordinate $z_c = 0.001$ m, (b) optimal nozzle y coordinate vs $Re_{in}$ for particle release z-coordinate $z_c = 0.02$ m, (c) optimal nozzle x coordinate vs $Re_{in}$ for particle release z-coordinate $z_c = 0.04$ m, and (d) confidence ellipses for data shown in (a), (b), and (c).

neither $Re_{in}$ nor the nozzle $z_c$ coordinate for particle release significantly impacts the optimal nozzle diameter range. Therefore, it can be concluded that (1) to determine the optimal nozzle location and release timing for maximizing drug delivery efficiency to the larynx and glottis for JORRP treatment, the aid of an AI algorithm (i.e., the present study) is essential; (2) furthermore, investigation is needed to learn the relationships between parameters mentioned above, by plotting the raw dataset provided in Appendix D (in the supplementary material) in other ways (see Sec. III A 3 and Fig. 15).

### 4. Optimal nozzle diameter for TD vs drug characteristics and human factors

The optimal nozzle diameter $D_{nozzle}$ plays a crucial role in targeted delivery, influencing both the ease and reliability of successfully implementing TDS in inhaler production and clinical use. To explore the impacts of drug properties (i.e., particle diameter) and human factors (i.e., inhalation and exhalation profile) on the optimal nozzle

diameter $D_{nozzle}$, Figs. 15(a)–15(i) illustrate the variations in nozzle diameter based on the parameters mentioned above at different particle release time and nozzle center $z_c$ coordinates. Specifically, the particle diameter $d_p$ ranges from 500 nm to 10 $\mu$m, the particle release time $t$ changes from t = 0 to t = 0.5 s, and the nozzle center $z_c$ coordinate varies from $z_c = 0.001$ to $z_c = 0.04$ m for all peak inhalation flow rates $Q_{max}$, which were used in this study. More detailed information on the parameters and their values can be found in Table I.

Figures 15(a)–15(i) show a common tendency is that the optimal nozzle diameter tends to rise along with the particle diameter with a few exceptions. This is because the orange particle release areas (see Fig. 11 as an example) for larger particle size (i.e., $d_p = 5$ and 10 $\mu$m) are much larger than those for smaller particle size, which enables larger available region for nozzle placement with larger optimal diameters. However, it is worth noting that the optimal nozzle diameter $D_{nozzle}$ is zero for the following cases, i.e., particles ($d_p = 10$ $\mu$m) with flow rates 52.5 and 60 l/min using release time stations at t = 0.25 and t = 0.5 s [see Figs. 15(c), 15(f), 15(h), and 15(i)]. This occurs because
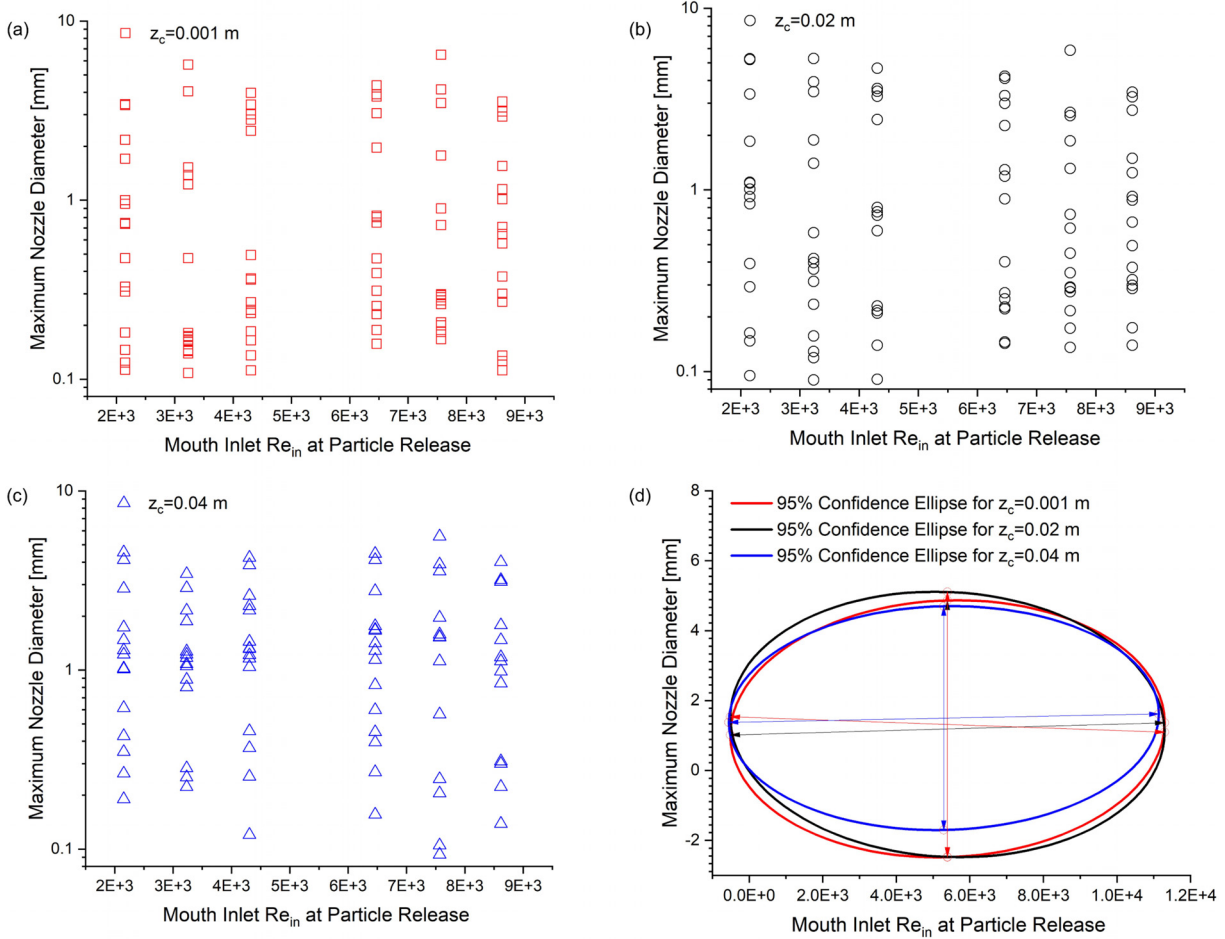
**FIG. 14.** Maximum nozzle diameter vs mouth inlet $Re_{in}$ at particle release time: (a) Maximum nozzle diameter vs $Re_{in}$ for particle release z-coordinate $z_c = 0.001$ m, (b) maximum nozzle diameter vs $Re_{in}$ for particle release z-coordinate $z_c = 0.02$ m, (c) maximum nozzle diameter vs $Re_{in}$ for particle release z-coordinate $z_c = 0.04$ m, and (d) confidence ellipses for data shown in (a)–(c).

that very few particles deposited in the targeting region (i.e., larynx and glottis) in those cases (see the particle local deposition patterns in Fig. 10), due to the relatively high $Re_{in}$ at particle release time and the resultant high inertial impaction for particle deposition in pharynx.

Additionally, Fig. 15 indicates that the optimal nozzle diameter tends to increase along with the particle release time (also see Appendix D in the supplementary material for the raw CFPD data) in most conditions. This trend indicates that releasing particles at t = 0.25 and t = 0.5 s during inhalation time tends to result in higher deposition and larger particle release region (i.e., orange region in particle release maps). Differences in some cases can also be observed in Figs. 15(b)–15(i) where the nozzle diameter increased from release time t = 0.0 to t = 0.25 s, then decreased at t = 0.5 s. Such observation indicates that enhancing particle deposition in larynx and glottis needs subtle inlet condition control to reach the optimal balance between inertial impaction and turbulence dispersion. Specifically, a higher $Re_{in}$ at the time of particle release results in a greater turbulence dispersion effect, which favors particle deposition in the larynx and glottis. Yet, simultaneously, a higher $Re_{in}$ during particle release can also enhance

inertial impaction, resulting in particle losses from deposition in regions like the oral cavity and pharynx, which are upstream of the targeted area for JORRP treatment. For instance, the reduction in optimal nozzle diameter $D_{nozzle}$ as the particle release time increases from t = 0.25 to 0.5 s shown in Figs. 15(b)–15(i) can be attributed to the heightened deposition and subsequent particle losses in the oral cavity and pharynx due to the rising $Re_{in}$. Among all CFPD simulation results, the maximum nozzle diameter was found for $d_p = 5\,\mu$m with the peak inhalation flow rate of 52.5 l/min, particle release time at t = 0.5 s, and nozzle center coordinate $z_c = 0.001$ m [see Fig. 15(c)].

Furthermore, Fig. 15 also unveils that the nozzle diameter changes as the particle injection z coordinate (i.e., $z_c$) changes for each peak inhalation flow rate and particle release time. The general trend can be seen is that the nozzle diameter $D_{nozzle}$ tends to increase as the nozzle position changes from $z_c = 0.001$ to $z_c = 0.04$ m, which is aligned with Fig. 14. However, a few different results are also seen for cases with $d_p = 10\,\mu$m particles in Figs. 15(c), 15(f), and 15(i), as $D_{nozzle}$ decreases with increasing $z_c$. Overall, particle size has more noticeable influence on the nozzle diameter as it is clearly found in
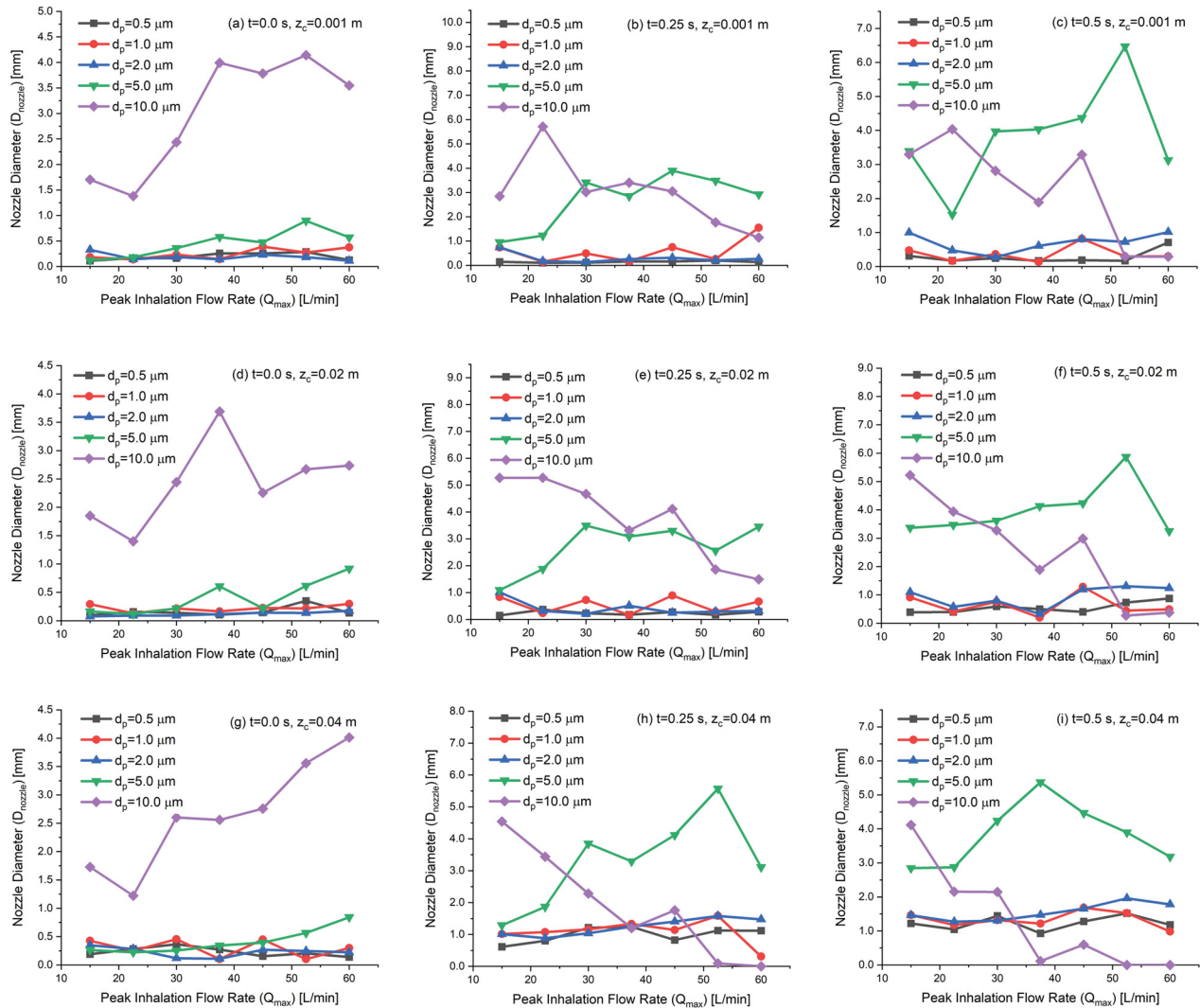
**FIG. 15.** Comparison of nozzle diameter depending on different parameters and in terms of peak inhalation flow rates at various release time (t) and release z-position ($z_c$): (a) $t = 0.0$ s, $z_c = 0.001$ m, (b) $t = 0.25$ s, $z_c = 0.001$ m, (c) $t = 0.50$ s, $z_c = 0.001$ m, (d) $t = 0.0$ s, $z_c = 0.02$ m, (e) $t = 0.25$ s, $z_c = 0.02$ m, (f) $t = 0.50$ s, $z_c = 0.02$ m, (g) $t = 0.0$ s, $z_c = 0.04$ m, (h) $t = 0.25$ s, $z_c = 0.04$ m, and (i) $t = 0.50$ s, $z_c = 0.04$ m.

Fig. 15 that smaller particle sizes ($d_p = 500$ nm, 1, and 2 $\mu$m) are showing very small nozzle diameters, whereas using 5 and 10 $\mu$m particles provides a good improvement in nozzle diameter $D_{nozzle}$. To facilitate the readers to understand Sec. III A 3, the raw CFPD data shown in Fig. 15 are provided in Appendix D in the supplementary material.

## B. ML Results

### 1. Targeted delivery efficiency vs conventional inhalation therapy efficiency

As shown in Figs. 1 and 2, the ML model was trained for outputting the optimal nozzle diameter $D_{nozzle}$, nozzle location ($x_c$, $y_c$, $z_c$), and particle release time ($t$) to achieve the highest targeted delivery

efficiency based on patient-specific and medication-specific inputs [i.e., peak inhalation flow rate ($Q_{max}$) and particle diameter ($d_p$)]. To evaluate the precision of ML output, Fig. 16 compares the DF results between the conventional inhalation therapy (i.e., full-mouth aerosol inhalation) and the targeted delivery strategy (TDS) developed based on ML or CFPD. As mentioned above, data shown in Fig. 16 demonstrate how well the targeted drug delivery efficiency to larynx and glottis using CFPD simulation with ML outputs, in comparison with targeted drug delivery determined solely by CFPD targeted delivery simulations. For this study, 315 simulation cases were run using various combinations of the listed parameters in Fig. 2. However, to keep one-to-one mapping between the input data and the corresponding continuous target values that can be used for CART model training, the training and testing dataset is reduced to 35 samples, using
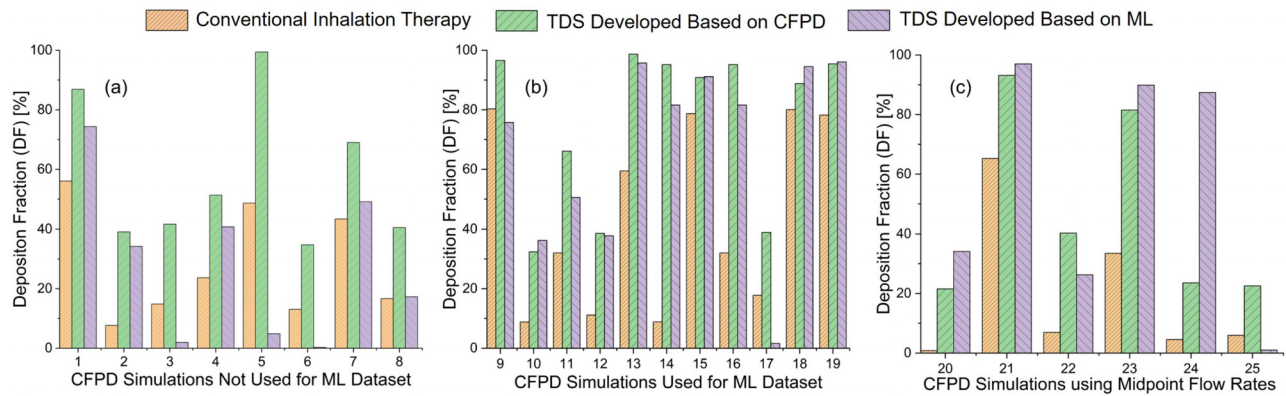
**FIG. 16.** DF comparisons at larynx and glottis among conventional inhalation therapy, TDS developed based on CFPD, and TDS developed based on ML: (a) CFPD simulation data that were not used for ML dataset, (b) CFPD simulation data from ML dataset, (c) CFPD simulation data considering midpoint inhalation flow rates.

constraints for filtration. Specifically, for each peak inhalation flow rate, five respective sample CFPD simulation datasets were chosen five different particle diameters, considering the maximum nozzle diameter and targeted delivery efficiency to larynx and glottis, irrespective of particle release time and position. Consequently, there are 35 data samples after using the constraint filtration mentioned above, with five for each inhalation flow rate.

In this section, three types of CFPD simulation data were used to evaluate the precision of the ML model in predicting targeted delivery, compared to CFPD predicted TDS and conventional inhalation therapy. Figure 16(a) shows the DF comparison for the CFPD simulation data, which were not used for ML training and testing. Sample data used for Fig. 16(a) were randomly selected from each of the peak inhalation flow rates. Therefore, other parameters, such as particle diameter $d_p$, particle release time $t$, and release $z_c$ position, are not the same as each other. Alternatively, Fig. 16(b) shows the DF comparison with selected CFPD simulation data, which were used for ML training and testing dataset. Finally, six additional peak inhalation flow rates were chosen as midpoint flow rates between each pair of the neighboring seven flow rates $Q_{max}$ used in this study (i.e., 18.75, 26.25, 33.75, 31.25, 48.75, and 56.25 l/min). The DFs across three types of drug particle delivery methods discussed in this study, including the conventional, trained ML models using CFPD results as inputs, and solely CFPD prediction strategy for targeted delivery, are compared and visualized in Fig. 16(c). A detailed summary of the boundary conditions used for the samples considered for Fig. 16 is also tabulated in Table IV.

Based on the DFs shown in Fig. 16 between conventional inhalation therapy, targeted delivery strategy (TDS) developed solely based on CFPD, and TDS based on ML, it is evident that both targeted delivery results show improvements in deposition at larynx and glottis (i.e., the targeted region) compared to the conventional inhalation therapy. Higher deposition in targeted regions is considered favorable as it indicates a more effective delivery of drug particles in diseased areas and less deposition in healthy tissues. Indeed, TDS developed solely based on CFPD simulations shows consistently higher DFs compared to the conventional inhalation therapy, as shown in Figs. 16(a)–16(c). The targeted delivery efficiency, i.e., DF at larynx and glottis, can reach close to 99.4%. This suggests that CFPD simulations help in achieving better drug delivery outcomes for these samples as better treatment for

**TABLE IV.** Details of the boundary conditions of the 25 samples used for DF's comparison.

| Sample | Peak inhalation flow rate, $Q_{max}$ (l/min) | Particle diameter, $d_p$ ($\mu$m) | Nozzle Z-coordinate, $z_c$ (m) | Particle release time, t (s) |
|---|---|---|---|---|
| 1 | 15 | 5 | 0.001 | 0.5 |
| 2 | 22.5 | 5 | 0.04 | 0.5 |
| 3 | 30 | 1 | 0.04 | 0.25 |
| 4 | 30 | 5 | 0.04 | 0.25 |
| 5 | 37.5 | 10 | 0.001 | 0.25 |
| 6 | 45 | 2 | 0.04 | 0.5 |
| 7 | 52.5 | 1 | 0.04 | 0.5 |
| 8 | 60 | 2 | 0.02 | 0.5 |
| 9 | 15 | 10 | 0.02 | 0.25 |
| 10 | 22.5 | 2 | 0.04 | 0.5 |
| 11 | 22.5 | 5 | 0.02 | 0.5 |
| 12 | 30 | 2 | 0.04 | 0.5 |
| 13 | 30 | 10 | 0.02 | 0.25 |
| 14 | 37.5 | 0.5 | 0.04 | 0.25 |
| 15 | 37.5 | 5 | 0.04 | 0.5 |
| 16 | 45 | 10 | 0.02 | 0.25 |
| 17 | 52.5 | 2 | 0.04 | 0.5 |
| 18 | 52.5 | 5 | 0.001 | 0.5 |
| 19 | 60 | 5 | 0.02 | 0.5 |
| 20 | 18.75 | 2 | 0.02 | 0 |
| 21 | 26.25 | 10 | 0.001 | 0.5 |
| 22 | 33.75 | 0.5 | 0.04 | 0.25 |
| 23 | 41.25 | 10 | 0.001 | 0.5 |
| 24 | 48.75 | 5 | 0.04 | 0 |
| 25 | 56.25 | 1 | 0.02 | 0.25 |

JORRP. This is likely because CFPD allows for a more accurate control and detailed simulation of particle trajectories based on first principles when using particle release maps, resulting in better targeted delivery efficiency to larynx and glottis. However, using TDS developed solely

based on CFPD is time-consuming, due to the high cost of computational time for patient-specific and disease-specific CFPD simulations. With much lower computational cost, the TDS based on ML model prediction shows varying results in comparison with TDS based solely on CFPD and conventional inhalation therapy. In some cases, TDS based on ML model prediction performs closely to TDS developed solely based on CFPD, indicating that the ML model has learned to approximate CFPD results effectively. In Fig. 16(b), sample cases 10, 12, 15, and 19 show almost similar DF predictions for both TDS based on ML model and TDS based solely on CFPD. However, in other cases, TDS based on ML model prediction shows lower DFs than TDS developed solely based on CFPD, i.e., all cases shown in Fig. 16(a). Such observations indicate that the predictive capability of the ML model is not always on par with TDS solely based on CFPD simulation in accuracy. It is also worth mentioning that sample data 3, 5, and 6 in Fig. 16(a) shows even less DFs for ML prediction compared to the conventional inhalation therapy. However, ML model prediction shows better performance in Fig. 16(c) with the DFs for sample cases 20, 21, 23, and 24 even higher than CFPD-based TDS. Overall, both the ML-predicted CFPD-based TDS and the CFPD solely based on TDS can significantly enhance the targeted delivery efficiency to larynx and glottis compared to the conventional inhalation therapy, indicating a potential enhancement in therapeutic outcome and reduced side effect.

### 2. ML model performance

To further analyze the success rate of the applied ML model to the CFPD dataset, this study sets up two threshold values as a measurement of the success. The threshold values are $RD \leq 15\%$ and $RD \leq 20\%$, where RD is the relative difference between DFs associated with different drug delivery strategies. The ML prediction is considered a success when the RD is not more than the specified number. The RD is measured with the DF of TDS based on ML model prediction compared with the DF of both conventional inhalation therapy and the DF of TDS developed solely based on CFPD. More details of RDs and the success rate are listed in Tables V and VI, as well as Fig. 17. The negative RDs in some cases indicate that the DF of TDS based on ML model prediction is higher than the DF of both conventional inhalation therapy and the DF of TDS developed solely based on CFPD.

Table V and Fig. 17(a) show the RDs in between the DF of TDS based on ML model prediction and the DF of conventional inhalation therapy. It is evident that ML model prediction gives better DF in almost all cases. In only five cases, the ML prediction fails to meet the threshold RD values. Despite those few inaccurate predictions, the success rate of the ML model is around 80% (see Table V) compared to conventional inhalation therapy. Such comparisons indicate that the TDS based on ML can successfully deliver aerosolized medications to larynx and glottis with higher DFs at least with a success rate of 80% than conventional inhalation therapy.

The comparison of DFs for TDS developed solely based on CFPD and TDS based on ML model based on the two threshold values is added in Table VI and Fig. 17(b). The success rate for ML model is 56% when the $RD \leq 15\%$, and it increases to around 60% when the RD threshold value is 20%. The comparison indicates that TDS based on ML provides similar or higher targeted delivery efficiencies in 56% or 60% cases when compared to the TDS developed solely based on CFPD. Although the success rate of TDS based on ML is not very high, it remains a preferred option for the targeted delivery, because it

**TABLE V.** The success rate of the ML model compared to conventional injection depending on one threshold value.

| Sample | DF of conventional injection (%) | DF of TD for ML prediction (%) | Relative differences (RD) (%) | $RD \leq 15$; acceptable (Y) or not acceptable (N) |
|---|---|---|---|---|
| 1 | 56.09 | 74.38 | −32.61 | Y |
| 2 | 7.67 | 34.24 | −346.43 | Y |
| 3 | 14.85 | 1.96 | 86.80 | N |
| 4 | 23.67 | 40.81 | −72.41 | Y |
| 5 | 48.70 | 4.85 | 90.05 | N |
| 6 | 13.06 | 0.30 | 97.70 | N |
| 7 | 43.42 | 49.12 | −13.11 | Y |
| 8 | 16.69 | 17.30 | −3.64 | Y |
| 9 | 80.32 | 75.75 | 5.69 | Y |
| 10 | 8.83 | 36.22 | −310.45 | Y |
| 11 | 32.03 | 50.54 | −57.78 | Y |
| 12 | 11.15 | 37.77 | −238.77 | Y |
| 13 | 59.45 | 95.70 | −60.97 | Y |
| 14 | 8.87 | 81.62 | −820.02 | Y |
| 15 | 78.73 | 91.13 | −15.75 | Y |
| 16 | 32.03 | 81.62 | −154.81 | Y |
| 17 | 17.76 | 1.60 | 91.00 | N |
| 18 | 80.05 | 94.53 | −18.08 | Y |
| 19 | 78.23 | 96.09 | −22.82 | Y |
| 20 | 0.79 | 34.12 | −4195.56 | Y |
| 21 | 65.24 | 97.00 | −48.67 | Y |
| 22 | 6.95 | 26.28 | −278.40 | Y |
| 23 | 33.49 | 89.89 | −168.45 | Y |
| 24 | 4.54 | 87.41 | −1826.85 | Y |
| 25 | 5.97 | 0.98 | 83.58 | N |
| Success rate (%) | | | | 80 |

can deliver drug to larynx and glottis more than the conventional inhalation therapy with a success rate of 80%.

Additionally, the ML model performances were also evaluated by a few evaluation metrics such as MSE, MAE, and $R^2$, depending on varying CV-fold value for the cross-validation (CV). Table VII listed those metrics values across different CV-fold numbers for both training and testing data. The MSE and MAE for the CV-fold with two on the training and testing data are low, and the $R^2$ is high for training data but very low for testing. This shows that the ML model does not generalize well to new data. The CV-fold with twelve has the lowest MSE and MAE with highest $R^2$ on the training data, but it also has the negative $R^2$, which means very worse prediction. The threefold CV appears to be a reasonable balance between precision and generalization though it has a comparatively high MSE and MAE on training data, but low on the testing data. The $R^2$ value for the training and testing dataset is 0.4778 and 0.7493, respectively. This indicates that the ML model explains 47.78% and 74.93% of the variation in the training data and in the testing data, respectively. The findings indicate that the ML model performs better on testing data than on training data,

**TABLE VI.** Success rate of the ML model compared to CFPD prediction depending on two threshold values.

| Sample | DF of TD for CFPD (%) | DF of TD for ML prediction (%) | Relative differences (RD) (%) | RD ≤ 15%; acceptable (Y) or not (N) | RD ≤ 20%; acceptable (Y) or not (N) |
|---|---|---|---|---|---|
| 1 | 86.91 | 74.38 | 14.42 | **Y** | **Y** |
| 2 | 39.09 | 34.24 | 12.42 | **Y** | **Y** |
| 3 | 41.66 | 1.96 | 95.30 | N | N |
| 4 | 51.35 | 40.81 | 20.52 | N | **Y** |
| 5 | 99.41 | 4.85 | 95.13 | N | N |
| 6 | 34.76 | 0.30 | 99.14 | N | N |
| 7 | 69.02 | 49.12 | 28.84 | N | N |
| 8 | 40.56 | 17.30 | 57.34 | N | N |
| 9 | 96.62 | 75.75 | 21.60 | N | N |
| 10 | 32.37 | 36.22 | −11.89 | **Y** | **Y** |
| 11 | 66.12 | 50.54 | 23.56 | N | N |
| 12 | 38.56 | 37.77 | 2.06 | **Y** | **Y** |
| 13 | 98.68 | 95.70 | 3.01 | **Y** | **Y** |
| 14 | 95.18 | 81.62 | 14.25 | **Y** | **Y** |
| 15 | 90.82 | 91.13 | −0.34 | **Y** | **Y** |
| 16 | 95.18 | 81.62 | 14.25 | **Y** | **Y** |
| 17 | 38.91 | 1.60 | 95.89 | N | N |
| 18 | 88.84 | 94.53 | −6.40 | **Y** | **Y** |
| 19 | 95.45 | 96.09 | −0.68 | **Y** | **Y** |
| 20 | 21.56 | 34.12 | −58.25 | **Y** | **Y** |
| 21 | 93.17 | 97.00 | −4.11 | **Y** | **Y** |
| 22 | 40.31 | 26.28 | 34.79 | N | N |
| 23 | 81.53 | 89.89 | −10.26 | **Y** | **Y** |
| 24 | 23.57 | 87.41 | −270.94 | **Y** | **Y** |
| 25 | 22.57 | 0.98 | 95.66 | N | N |
| | | Success rate (%) | | 50 | 57.14 |
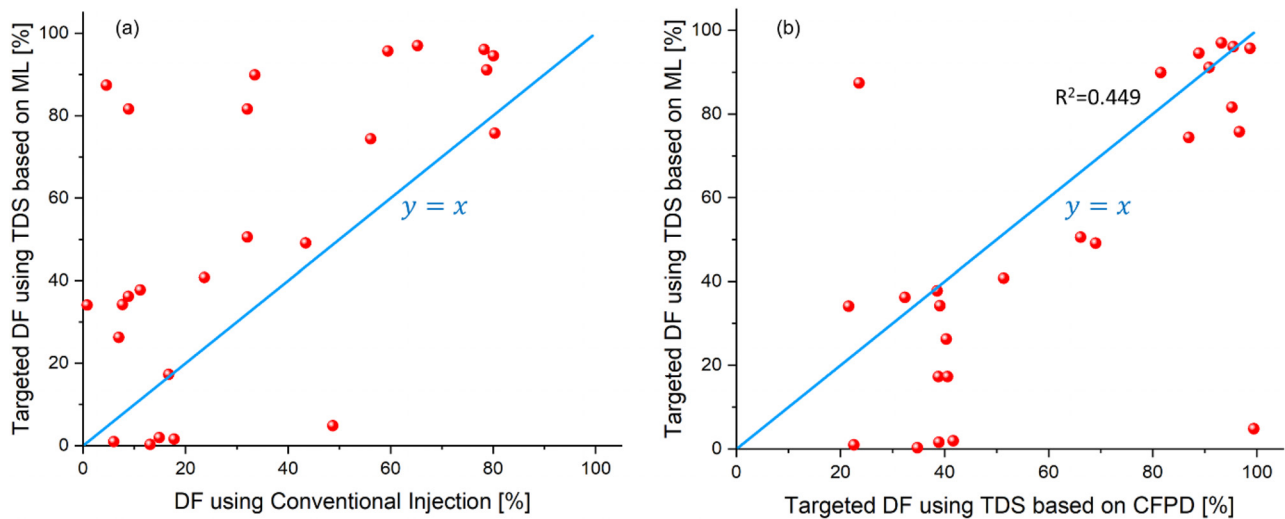


**FIG. 17.** 2D scatter plots of DFs in larynx and glottis using different drug administration strategies: (a) Targeted DF using TDS based on ML vs DF using conventional inhalation therapy (see Table V), and (b) Targeted DF using TDS based on ML vs Targeted DF using TDS based on CFPD (see Table VI).

**TABLE VII.** ML model performance based on different CV values.

| CV | Training data | | | Testing data | | |
| --- | --- | --- | --- | --- | --- | --- |
| | MSE | MAE | $R^2$ | MSE | MAE | $R^2$ |
| 2 | 0.0014 | 0.0129 | 0.5972 | 0.0001 | 0.0028 | 0.0146 |
| **3** | **0.0018** | **0.0156** | **0.4778** | **0.0001** | **0.0022** | **0.7493** |
| 5 | 0.0014 | 0.0130 | 0.5057 | 0.0001 | 0.0029 | 0.6545 |
| 10 | 0.0014 | 0.0130 | 0.5874 | 0.0001 | 0.0028 | 0.0036 |
| 12 | 0.0006 | 0.0056 | 0.7559 | 0.0001 | 0.0040 | −1.8407 |
| 15 | 0.0014 | 0.0130 | 0.5057 | 0.0001 | 0.0029 | 0.6545 |

demonstrating that the model is not overfitted and that it generalizes well to new data.

In summary, the TDS based on ML model significantly outperforms the conventional inhalation therapy in terms of particle delivered dose to the targeted region, meaning no or less side effects on healthy tissues. On the other hand, the TDS based on ML model is not up to the level of TDS developed solely based on CFPD. However, the TDS based on ML model is still somehow comparable to TDS developed solely based on CFPD in targeted delivery efficiency with much lower computational cost. Both TDS methods showed improved drug delivery to the larynx and glottis than conventional inhalation therapy, which will provide for better JORRP treatment.

## IV. CONCLUSIONS

This study proposed and developed a physics-informed ML model for TDS development for JORRP treatment, utilizing the CFPD simulation data to investigate the feasibility of delivering the drug particles precisely to the JORRP affected region, specifically to the larynx and glottis. TDS based on ML model can provide the optimal nozzle location and nozzle diameter as well as the particle release time to precisely control the aerosolized particle release to achieve the targeted drug delivery, according to the patient-specific inhalation information and drug particle sizes. This capability enables more effective drug particle delivery to the designated airway sites (i.e., larynx and glottis), while minimizing the deposition on the healthy tissues. Such a ML model can be potentially integrated into a user-centered smart inhaler to achieve personalized targeted delivery for precise JORRP treatment. Additionally, the ML model can be further trained with targeted drug delivery dataset for other chronic lung diseases to deliver drugs to other specific designated pulmonary sites. Based on the analysis of CFPD and ML data and performance, key conclusions of this study are listed below, i.e.,

(1) Inhaled particle size has significant influence on DFs in upper airway, and the resultant particle release map patterns and the easiness of targeted delivery. Larger particles (i.e., $d_p = 10 \ \mu$m) have enhanced inertial impaction, which leads to concentrated particle deposition in the oral cavity and pharynx, and nearly no deposition at larynx and glottis.

(2) Larger optimal nozzle diameter as well as higher targeted delivery efficiencies to the larynx and glottis region was found in most of the cases for larger particles (i.e., 5 and 10 $\mu$m), although the flow rates, particle release time, and particle release $z_c$ position are changing. However, a few exception cases were

also seen, indicating a need for further study to find a better correlation between the investigated factors and the possible nozzle diameter.

(3) Both the peak inhalation flow rate and particle release time show noticeable impact on the configuration of particle release maps, thereby influencing the inhaler nozzle diameter and the injection position. At a release time of t = 0.0 s, an increase in peak inhalation flow rate leads to a larger nozzle diameter because of the enhanced turbulence dispersion due to the higher inhalation flow rate and the inlet Reynolds number. On the other hand, for release times at t = 0.25 and 0.5 s, an increasing flow rate results in a smaller nozzle diameter. This is due to the further enhanced inertial impaction, which leads to a major loss of drug particles due to the deposition in oral cavity and pharynx before reaching larynx and glottis. Therefore, an appropriate inlet Reynolds number at the time of particle release is important for achieving optimal targeted delivery to larynx and glottis.

(4) In comparison with other ML regression models, the CART model shows more accurate results, with the best accuracy found with MSE, MAE, and $R^2$. The $R^2$ values clearly indicate that the sample size is not high enough for high ML model accuracy, despite their low MSE and MAE values.

(5) Given the constrained size of the training and testing datasets, two distinct threshold values were established to assess the performance of the ML model in achieving successful targeted delivery. The findings indicate that the ML CART model facilitates a notable enhancement in particle delivery to the larynx and glottis compared to conventional inhalation therapy, showing an 80% success rate in deposition fraction comparisons. Additionally, in approximately 60% of the case comparisons, the ML CART model yielded deposition fractions comparable to TDS developed solely based on CFPD. Consequently, the ML CART model devised in this study holds promise for shaping patient-specific and medication-specific targeted delivery strategies, paving the way for minimized side effects, optimized therapeutic results, and a more cost-efficient and expedient approach.

## V. LIMITATIONS OF THIS STUDY AND FUTURE WORK

The simplifications and assumptions of this study are as follows:

(1) During actuation, significant changes in temperature may take place while using inhaler resulting in thermophoretic influences on particles,[46] as well as droplet size change due to evaporation/condensation.

(2) This study utilized one-way air-particle coupling, neglecting the influence of particle presence on airflow field or particle–particle interactions such as agglomeration/de-agglomeration.[47]

(3) Monodisperse aerosols and mean particle diameters were employed in CFPD simulations instead of more realistic polydisperse particle size distributions.[48]

(4) The deformation kinematics of tongue, glottal aperture, and lungs were neglected in this study.[49]

(5) The impact of cilia-driven mucus motion on drug removal was not taken into account in the study.[50]

24 February 2024 07:06:57

(6) The dataset used for training and testing the ML CART model is currently limited (see Fig. 1 and Sec. III B 1), offering potential for expansion in future studies.

To address the above-mentioned simplification and assumptions, future work includes:

(1) Explore the temperature and relative humidity changes in human respiratory system as well as their effect on particle/droplet size change and transport dynamics.
(2) Include more realistic polydisperse particle size distributions in future CFPD simulations.
(3) Develop a geometrical model having a realistic dynamic airway motion for the future CFPD study.
(4) Employ two-way coupled Euler–Lagrange method or discrete element method (DEM) and will be included to enable the simulation of realistic particle–airflow interactions and particle–particle interactions.
(5) Develop a multiscale numerical approach, integrating CFPD with the discrete element method (DEM), will be employed to explicitly simulate cilia motion-driven mucus movement to examine the impact of mucus clearance on drug delivery using flexible fiber model.[51]
(6) Augment the training and testing data with expanded CFPD simulations on targeted drug delivery by considering additional factors such as inter-subject variability in anatomy and disease-specific lung environment. Additionally, employing a broader range of ML and DL algorithms could further enhance the efficiency of inhaler drug delivery.

## SUPPLEMENTARY MATERIAL

See the supplementary material for Appendix A: Dataset Used for the ML Model Training and Testing (After Filtration); Appendix B: The CART Model Implementation and Optimization; Appendix C: Particle Number Independence Test; Appendix D: Complete Dataset for ML Training and Testing (315 CFPD Simulations).

## ACKNOWLEDGMENTS

## AUTHOR DECLARATIONS
### Conflict of Interest

The authors have no conflicts to disclose.

### Author Contributions

**Mohammad Rashedul Islam:** Conceptualization (equal); Data curation (equal); Formal analysis (equal); Investigation (equal); Methodology (equal); Project administration (equal); Resources (equal); Software (equal); Validation (equal); Visualization (equal); Writing – original draft (equal); Writing – review & editing (equal). **Chenang Liu:** Conceptualization (equal); Funding acquisition (equal); Methodology (equal); Writing – review & editing (equal). **Chanjie Cai:** Data curation (equal); Methodology (equal); Writing – review & editing (equal). **Jindal K. Shah:** Conceptualization (equal); Data curation (equal); Methodology (equal); Supervision (equal). **Yu Feng:** Conceptualization (equal); Data curation (equal); Formal analysis (equal); Funding acquisition (equal); Investigation (equal); Methodology (equal); Project administration (equal); Resources (equal); Software (equal); Supervision (equal); Visualization (equal); Writing – review & editing (equal).

## DATA AVAILABILITY

The data that support the findings of this study are available from the corresponding author upon reasonable request.

## REFERENCES

[1]A. H. Morgan and R. P. Zitsch, "Recurrent respiratory papillomatosis in children: A retrospective study of management and complications," Ear Nose Throat J. **65**(9), 19–28 (1986).

[2]C. S. Derkay and B. Wiatrak, "Recurrent respiratory papillomatosis: A review," Laryngoscope **118**(7), 1236–1247 (2008).

[3]C. J. Lacey, C. M. Lowndes, and K. V. Shah, "Burden and management of non-cancerous HPV-related conditions: HPV-6/11 disease," Vaccine **24**, S35–S41 (2006).

[4]F. J. Buchinsky et al., "Age of child, more than HPV type, is associated with clinical course in recurrent respiratory papillomatosis," PloS One **3**(5), e2263 (2008).

[5]S. Dodhia et al., "Investigation of the presence of HPV on KTP laser fibers following KTP laser treatment of papilloma," Laryngoscope **128**(4), 926–928 (2018).

[6]S. Florian Preuss et al., "Long-term results of surgical treatment for recurrent respiratory papillomatosis," Acta Oto-Laryngol. **127**(11), 1196–1201 (2007).

[7]D. J. Wellenstein et al., "Office-based $CO_2$ laser surgery for benign and premalignant laryngeal lesions," Laryngoscope **130**(6), 1503–1507 (2020).

[8]J. R. Lechien, J. A. Burns, and L. M. Akst, "The use of 532-Nanometer-pulsed potassium-titanyl-phosphate (KTP) laser in laryngology: A systematic review of current indications, safety, and voice outcomes," Ear. Nose Throat J. **100**(1 suppl), 4S–13S (2021).

[9]C. S. Derkay and A. E. Bluher, "Update on recurrent respiratory papillomatosis," Otolaryngol. Clin. North Am. **52**(4), 669–679 (2019).

[10]B. Coulombeau et al., "Anti-viral injectable treatment (cidofovir) in laryngeal papillomatosis," Rev. Laryngol., Otol., Rhinol. **123**(5), 315–320 (2002).

[11]E. P. Kiell and S. E. Sobol, "Malignant transformation and distal airway complications," in *Recurrent Respiratory Papillomatosis* (Springer, 2018), pp. 153–166.

[12]C. S. Derkay, "Task force on recurrent respiratory papillomas: A preliminary report," Arch. Otolaryngol.–Head Neck Surg. **121**(12), 1386–1391 (1995).

[13]B. G. Leventhal et al., "Randomized surgical adjuvant trial of interferon Alfa-n1 in recurrent papillomatosis," Arch. Otolaryngol.–Head Neck Surg. **114**(10), 1163–1169 (1988).

[14]G. B. Healy et al., "Treatment of recurrent respiratory papillomatosis with human leukocyte interferon," N. Engl. J. Med. **319**(7), 401–407 (1988).

[15]C. A. Rosen and P. C. Bryson, "Indole-3-carbinol for recurrent respiratory papillomatosis: Long-term results," J. Voice **18**(2), 248–253 (2004).

[16]C. Kleinstreuer and Z. Zhang, "Airflow and particle transport in the human respiratory system," Annu. Rev. Fluid Mech. **42**, 301–334 (2010).

[17]C. Kleinstreuer and Z. Zhang, "Targeted drug aerosol deposition analysis for a four-generation lung airway model with hemispherical tumors," J. Biomech. Eng. **125**(2), 197–206 (2003).

[18]Y. Feng, X. Chen, and M. Yang, "An *in silico* investigation of a lobe-specific targeted pulmonary drug delivery method," in *Frontiers in Biomedical Devices* (American Society of Mechanical Engineers, 2018).

[19]C. Plank, "Nanomagnetosols: Magnetism opens up new perspectives for targeted aerosol delivery to the lung," Trends Biotechnol. **26**(2), 59–63 (2008).

[20]S. Kenjereš and J. L. Tjin, "Numerical simulations of targeted delivery of magnetic drug aerosols in the human upper and central respiratory system: A validation study," R. Soc. Open Sci. **4**(12), 170873 (2017).

[21]A. Ghosh, M. S. Islam, and S. C. Saha, "Targeted drug delivery of magnetic nano-particle in the specific lung region," Computation **8**(1), 10 (2020).

[22]Y. Ostrovski, P. Hofemeier, and J. Sznitman, "Augmenting regional and targeted delivery in the pulmonary acinus using magnetic particles," Int. J. Nanomed. **11**, 3385–3395 (2016).

[23]Y. Ostrovski et al., "Targeted drug delivery to upper airways using a pulsed aerosol bolus and inhaled volume tracking method," Flow Turbul. Combust. **102**(1), 73–87 (2019).

[24]M. R. Islam and Y. Feng, "Achieving targeted delivery of chemotherapeutic particles to small airway tumors via pulmonary route using endotracheal catheters: A CFPD study," Pharmaceuticals **16**(2), 158 (2023).

[25]J. Wang et al., "Targeted delivery of inhalable drug particles in a patient-specific tracheobronchial tree with moderate COVID-19: A numerical study," Powder Technol. **405**, 117520 (2022).

[26]F. Lavorini, M. Pistolesi, and O. S. Usmani, "Recent advances in capsule-based dry powder inhaler technology," Multidiscip. Respir. Med. **12**(1), 11 (2017).

[27]J. N. Pritchard and C. Nicholls, "Emerging technologies for electronic monitoring of adherence, inhaler competence, and true adherence," J. Aerosol Med. Pulm. Drug Delivery **28**(2), 69–81 (2015).

[28]T. Daniels et al., "Accurate assessment of adherence: Self-report and clinician report vs electronic monitoring of nebulizers," Chest **140**(2), 425–432 (2011).

[29]O. S. Usmani et al., "Critical inhaler errors in asthma and COPD: A systematic review of impact on health outcomes," Respir. Res. **19**(1), 1–20 (2018).

[30]C. Zabczyk and J. D. Blakey, "The effect of connected "smart" inhalers on medication adherence," Front. Med. Technol. **3**, 657321 (2021).

[31]D. Kikidis et al., "The digital asthma patient: The history and future of inhaler based health monitoring devices," J. Aerosol Med. Pulm. Drug Delivery **29**(3), 219–232 (2016).

[32]Z. Zhang, C. Kleinstreuer, and S. Hyun, "Size-change and deposition of conventional and composite cigarette smoke particles during inhalation in a subject-specific airway model," J. Aerosol Sci. **46**, 34–52 (2012).

[33]Y. Feng et al., "Tutorial: Understanding the transport, deposition, and translocation of particles in human respiratory systems using computational fluid-particle dynamics and physiologically based toxicokinetic models," J. Aerosol Sci. **151**, 105672 (2021).

[34]X. Chen et al., "Numerical investigation of particle deposition in a triple bifurcation airway due to gravitational sedimentation and inertial impaction," Powder Technol. **323**, 284–293 (2018).

[35]S. Morsi and A. Alexander, "An investigation of particle trajectories in two-phase flow systems," J. Fluid Mech. **55**(2), 193–208 (1972).

[36]M. D. Allen and O. G. Raabe, "Slip correction measurements of spherical solid aerosol particles in an improved Millikan apparatus," Aerosol Sci. Technol. **4**(3), 269–286 (1985).

[37]G. Kallio and M. Reeks, "A numerical simulation of particle deposition in turbulent boundary layers," Int. J. Multiphase Flow **15**(3), 433–446 (1989).

[38]A. Li and G. Ahmadi, "Dispersion and deposition of spherical particles from point sources in a turbulent channel flow," Aerosol Sci. Technol. **16**(4), 209–226 (1992).

[39]Y. Feng et al., "Computational transport, phase change and deposition analysis of inhaled multicomponent droplet–vapor mixtures in an idealized human upper lung model," J. Aerosol Sci. **96**, 96–123 (2016).

[40]Y. Feng, C. Kleinstreuer, and A. Rostami, "Evaporation and condensation of multicomponent electronic cigarette droplets and conventional cigarette smoke particles in an idealized G3–G6 triple bifurcating unit," J. Aerosol Sci. **80**, 58–74 (2015).

[41]A. Haghnegahdar, J. Zhao, and Y. Feng, "Lung aerosol dynamics of airborne influenza A virus-laden droplets and the resultant immune system responses: An in silico study," J. Aerosol Sci. **134**, 34 (2019).

[42]Y. Feng et al., "An in silico subject-variability study of upper airway morphological influence on the airflow regime in a tracheobronchial tree," Bioengineering **4**(4), 90 (2017).

[43]L. Breiman, J. Friedman, R. A. Olshen, and C. J. Stone, *Classification and Regression Trees* (Routledge, 1984).

[44]F. Gorunescu, *Data Mining: Concepts, Models and Techniques* (Springer Science & Business Media, 2011), Vol. 12.

[45]G. M. Barnas et al., "Influence of waveform and analysis technique on lung and chest wall properties," Respir. Physiol. **96**(2–3), 331–344 (1994).

[46]Z.-Q. Yin et al., "Thermophoresis and Brownian motion effects on nanoparticle deposition inside a 90 square bend tube," Aerosol Air Qual. Res. **18**(7), 1746–1755 (2018).

[47]S. Elghobashi and G. Truesdell, "On the two-way interaction between homogeneous turbulence and dispersed solid particles. I: Turbulence modification," Phys. Fluids A **5**(7), 1790–1801 (1993).

[48]M. Talaat et al., "Count- and mass-based dosimetry of MDI spray droplets with polydisperse and monodisperse size distributions," Int. J. Pharm. **623**, 121920 (2022).

[49]J. Zhao, Y. Feng, and C. A. Fromen, "Glottis motion effects on the particle transport and deposition in a subject-specific mouth-to-trachea model: A CFPD study," Comput. Biol. Med. **116**, 103532 (2020).

[50]H. Yi, Q. Wang, and Y. Feng, "Computational analysis of obstructive disease and cough intensity effects on the mucus transport and clearance in an idealized upper airway model using the volume of fluid method," Phys. Fluids **33**(2), 021903 (2021).

[51]A. Haghnegahdar, R. Bharadwaj, and Y. Feng, "Exploring the role of nasal hair in inhaled airflow and coarse dust particle dynamics in a nasal cavity: A CFD-DEM study," Powder Technol. **427**, 118710 (2023).

24 February 2024 07:06:57